RESEARCH ARTICLE | MAY 06 2024

# Influence of the tip speed ratio on the wake dynamics and recovery of axial-flow turbines

Antonio Posa ; Ignazio Maria Viola ; Riccardo Broglia



*Physics of Fluids* 36, 055109 (2024)
https://doi.org/10.1063/5.0203285

Physics of Fluids ARTICLE pubs.aip.org/aip/pof

# Influence of the tip speed ratio on the wake dynamics and recovery of axial-flow turbines

Cite as: Phys. Fluids **36**, 055109 (2024); doi: 10.1063/5.0203285
Submitted: 12 February 2024 · Accepted: 17 April 2024 ·
Published Online: 6 May 2024



Antonio Posa,[1,a)] Ignazio Maria Viola,[2] and Riccardo Broglia[1]

## AFFILIATIONS

[1]CNR-INM, Institute of Marine Engineering, National Research Council of Italy, Via di Vallerano 139, 00128 Roma, Italy
[2]The University of Edinburgh, School of Engineering, Institute of Energy Systems, Edinburgh, Scotland

[a)]Author to whom correspondence should be addressed: antonio.posa@cnr.it

## ABSTRACT

Detached eddy simulation is employed to investigate the wake development downstream of the rotor of an axial-flow turbine and its dependence on the tip speed ratio. In this study, we found that the trend of the momentum deficit as a function of the rotational speed shows opposite directions in the near wake and further downstream. While the momentum deficit in the near wake increases with the rotational speed, it decreases further downstream. For instance, we found that at six diameters downstream of the rotor the streamwise velocity in its wake recovered to about 30% of its free-stream value at the lowest simulated tip speed ratio of 4, while its recovery was equal to about 65% at the largest tip speed ratio of 10. This is due to the earlier breakdown of the tip vortices. The results of the computations demonstrate indeed that mutual inductance phenomena between tip vortices, promoting pairing events and the eventual instability of the helical structures, occur at shorter downstream distances for higher values of tip speed ratio. Wake instability enhances the process of wake recovery, especially due to radial advection. Therefore, higher rotational speeds do not promote wake recovery through more intense tip vortices, but through their greater instability. Implications are important, affecting the optimal distance between rows of axial-flow turbines in array configurations: the operation at higher rotational speeds allows for smaller distances between turbines, decreasing the cost and environmental impact of farms consisting of several devices.





## I. INTRODUCTION

The wake development of axial-flow, drag-generating rotors is of critical importance: it affects the speed of the momentum recovery downstream of them. This is the case, for instance, of the axial-flow turbines widely utilized in both fields of wind and hydrokinetic energy. These devices are usually required to operate in farm configurations. This is problematic, since interference among turbines is usually detrimental to their performance. Therefore, the design of farms or arrays requires proper optimization.[1–7] Downstream rows ingest the flow coming from the upstream devices, resulting in lower performance, in comparison with the same device operating in isolation, due to a reduction of the momentum available at their inflow.[6–12] Therefore, the ability to predict the length of the wake development downstream of axial-flow rotors and the speed of the process of wake recovery is especially critical for the selection of the mutual distance between devices. This choice is a function of the rotational speed, which affects the extent of the wake signature.

In the present study, we focus on the influence of the tip speed ratio, $\lambda$, of the rotor of an axial-flow turbine, representing its rotational speed in non-dimensional form, on the speed of its wake recovery. In our earlier studies, we have analyzed the dependence of the process of wake recovery on the stability of the tip vortices shed by a similar turbine.[13–15] Here, we will show that the speed of this process is substantially affected by $\lambda$. This has important implications on the selection of the relative distance between devices in array configurations, depending on their expected working conditions.

Since the instability of the tip vortices is believed to be the trigger of the process of momentum replenishment downstream of axial-flow rotors,[16–19] their accurate simulation in numerical studies is critical to properly reconstruct the correlation of their dynamics with the speed of wake recovery. The need of resolving the dynamics of the tip vortices results in a large computational cost of high-fidelity simulations: (i) they require fine levels of resolution in both space and time, resulting in a large count of grid nodes; (ii) since they are typically adopted to resolve the wake dynamics, their fine resolution needs to be extended to wider downstream distances; (iii) since they are targeted at resolving the unsteady dynamics of the wake, they need a long advancement in time. In addition, if the simulation of multiple operative conditions is

required, to explore the dependence on the tip speed ratio, as in the present study, the computational burden becomes even more challenging. Therefore, although a number of blade-resolving Reynolds-averaged Navier–Stokes (RANS) computations,[20–32] detached eddy simulations (DES),[25,27–29,33–36] and large eddy simulations (LES),[13–15,37–47] dealing with the wake development of axial-flow turbines, is currently available in the literature (see Niebuhr *et al.*[48] for a recent review), systematic studies dealing with the influence of $\lambda$ on the process of wake recovery of axial-flow rotors are uncommon. Furthermore, the analysis of the influence of $\lambda$ is often limited to the parameters of global performance of the turbine. In this work, we exploit well-resolved DES to capture the phenomena of mutual inductance between tip vortices, their resulting instability and their correlation with the process of wake recovery across a range of values of $\lambda$. The dynamics of the tip vortices is captured by means of an overlapping grids strategy, clustering grid cells at the outer boundary of the wake.

One of the most advanced studies in the field is the recent work by El Fajri *et al.*,[49] who adopted both RANS and DES to analyze the wake of a three-bladed turbine. They utilized a rotating mesh consisting of $3.5 \times 10^6$ cells in the framework of a finite-volume methodology to discretize the region of space surrounding the turbine and an additional, stationary grid consisting of $14.4 \times 10^6$ cells, encompassing the nacelle and the stanchion. Their analysis confirmed DES to be well suited to capture properly the process of instability of the tip vortices. As expected, RANS promoted their faster dissipation and was unable to predict their coupling and following breakdown into turbulence. DES verified a faster coupling and instability of the tip vortices for increasing values of $\lambda$, ranging between 2.00 and 6.15, although the study of sensitivity to $\lambda$ was carried out on a coarser grid of $7 \times 10^6$ cells.

RANS computations dealing with an axial-flow hydrokinetic turbine were conducted by Tian *et al.*,[50] with the purpose of analyzing the sensitivity to tip speed ratio, turbulence intensity at the inflow, and yaw angle. A grid consisting of $8 \times 10^6$ finite volumes was adopted. Although a few details on the wake features were provided, the analysis was actually focused on the global performance of the turbine, with limited information on the process of wake recovery. A RANS study was also reported by García Regodeseves and Santolaria Morros,[51] who carried out computations for three values of the tip speed ratio of a horizontal axis wind turbine, using a multi-block hexahedral mesh consisting of an overall number of $37.5 \times 10^6$ finite volumes. Increasing values of $\lambda$ resulted in a smaller pitch of the tip vortices, their faster instability and a faster recovery of momentum downstream of the turbine. However, a systematic analysis of the process of wake recovery and its correlation with the dynamics of the tip vortices was not conducted. A similar study was carried out by Siddiqui *et al.*[52] They simulated a small wind turbine by RANS on computational grids up to $4.0 \times 10^6$ cells, using both the sliding mesh interface and multiple reference frame techniques to handle the multiple parts of the turbine in relative motion. Although three values of tip speed ratio were simulated, an analysis of its influence on the process of wake recovery was not discussed.

A recent study, based on particle imaging velocimetry (PIV) measurements, was conducted by Di Felice *et al.*,[53] where the performance of a tidal turbine and the near wake evolution of its tip vortices were analyzed as functions of the tip speed ratio. Details including transport and production of turbulent kinetic energy were reported, besides first-order statistics of the wake flow, correlating them with the process of instability of the tip vortices. However, the analysis was limited to less than a diameter downstream of the rotor of the turbine and the process of wake recovery occurring at more downstream coordinates was not investigated. PIV was also adopted by Bourhis *et al.*[54] to assess the Reynolds number effects on the performance of a micro wind energy harvester, but in this study the analysis was especially focused on the performance of the turbine, rather than on its wake features. The recent PIV experiments by Biswas and Buxton[55] were conducted on a model-scale wind turbine at two different values of tip speed ratio, finding its strong influence on the dynamics of the tip vortices in the wake. They revealed that the pairing mechanisms of the tip vortices was characterized by a two-step process at the lower tip speed ratio, as the one observed by earlier experiments dealing with the wake of marine propellers.[56] In contrast, at the larger tip speed ratio the tip vortices shed by the three blades of the turbine appeared to merge more quickly through a single-step process.

The survey above demonstrates that studies dealing with the analysis of the correlation of the speed of wake recovery with the phenomena of instability of the tip vortices and the tip speed ratio are very limited in the literature, even when high-fidelity approaches are adopted. This limitation is tied to two major issues: (i) the focus is often on the performance of the rotor, rather than on the correlation between wake features and performance; (ii) in some studies an analysis of the wake dynamics is included, but it spans only a narrow range of values of $\lambda$. In this work, we contribute to the understanding of the problem by means of blade-resolving, DES computations, across a wide range of values of $\lambda$. This allows us exploring its influence on the wake instability and the resulting recovery, through a detailed discussion on the phenomena of coupling between tip vortices and their eventual breakdown, starting the process of momentum replenishment of the wake core from the free stream. Details are included through an analysis of each term of the momentum balance equation. We find that, despite the increasing momentum deficit in the near wake for higher values of $\lambda$, the wake recovery is actually faster, due to the earlier breakup of the wake coherence. This phenomenon allows the development of inward radial flows, bringing momentum from the free-stream into the wake core. This behavior of the wake flow has important implications in the interaction between streamlined turbines in farms, since the downstream devices ingest the flow coming from the upstream ones: a faster instability of the wake and its recovery at higher values of tip speed ratio are beneficial to the closer spacing between turbines in array configurations. These conclusions are achieved by using one of the most well-resolved DES computations to date, where a grid consisting of almost $36 \times 10^6$ cells is utilized in the framework of a finite-volume formulation. Overlapping grids allow clustering points in the regions of interest of the domain, especially the boundary layer of the blades and the outer region of the wake, populated by the tip vortices shed by the rotor.

In the following, we provide details on the numerical methodology (Sec. II), the computational setup (Sec. III), the analysis of the results (Sec. IV), and the final conclusions of this study (Sec. V).

## II. METHODOLOGY

The Navier–Stokes equations for incompressible, Newtonian fluids were resolved using a DES approach, implemented within a solver developed in-house at CNR-INM.[57–59]

The governing equations in non-dimensional form can be expressed as

$$\begin{cases} \dfrac{\partial u_i}{\partial x_i} = 0, \\ \dfrac{\partial u_i}{\partial t} + \dfrac{\partial u_i u_j}{\partial x_j} = -\dfrac{\partial p}{\partial x_i} + \dfrac{\partial \tau_{ij}}{\partial x_j} \quad \text{for } i = 1, 2, 3, \end{cases} \tag{1}$$

where $p$ and $u_i$ (for $i = 1, 2, 3$) are the state variables for incompressible flows, i.e., pressure and the velocity components across the three coordinate directions, while

$$\tau_{ij} = \left(\frac{1}{Re} + \nu_t\right)\left(\frac{\partial u_i}{\partial x_j} + \frac{\partial u_j}{\partial x_i}\right) \tag{2}$$

is the stress tensor. In Eq. (2), $Re$ is the Reynolds number, defined as $Re = \hat{L}\hat{V}/\hat{\nu}$, where $\hat{L}$ and $\hat{V}$ are the length and velocity reference scales, respectively, and $\hat{\nu}$ is the kinematic viscosity of the fluid (all dimensional quantities will be indicated with $\hat{\cdot}$). $\nu_t$ is the turbulent viscosity, which was computed via a DES approach based on the one-equation, Spalart–Allmaras turbulence model.[60,61] This resolves a transport equation for an auxiliary variable, $\tilde{\nu}$,

$$\frac{D\tilde{\nu}}{Dt} = \frac{1}{\sigma}\left\{\frac{\partial}{\partial x_j}\left[(\nu + \nu_T)\frac{\partial \tilde{\nu}}{\partial x_j}\right] + c_{b2}\frac{\partial \tilde{\nu}}{\partial x_j}\frac{\partial \tilde{\nu}}{\partial x_j}\right\} + c_{b1}[1 - f_{t2}]\tilde{S}\tilde{\nu} - \left[c_{w1}f_w - \frac{c_{b1}}{k^2}f_{t2}\right]\left(\frac{\tilde{\nu}}{d}\right)^2, \tag{3}$$

with $\nu_T = \tilde{\nu} f_{v1}$, being

$$f_{v1} = \frac{\chi^3}{\chi^3 + C_{v1}^3} \quad \text{where } \chi = \frac{\tilde{\nu}}{\nu}. \tag{4}$$

In Eqs. (3) and (4), $\tilde{S} = \mathscr{R} + \tilde{\nu} f_{v2}/(\kappa d)^2$, where $\mathscr{R} = 2\sqrt{\mathscr{R}_{ij}\mathscr{R}_{ij}}$, $\mathscr{R}_{ij}$ is the rotation tensor, and $d$ is the distance from the closest wall. All other functions and constants in these equations are defined as in the original paper by Spalart and Allmaras.[60]

In the DES approach, away from the solid walls the model automatically switches to a large eddy simulation (LES) approach, with the purpose of resolving the dynamics of the larger eddies. In the Spalart–Allmaras DES, this is accomplished by replacing the distance from the closest wall $d$ in Eq. (3) by a new function $\tilde{d}$, defined as

$$\tilde{d} = \min(d, C_{\mathrm{DES}}\Delta), \tag{5}$$

where $\Delta$ is the maximum size of the cells along the three directions in space (i.e., $\Delta = \max[dx, dy, dz]$), and $C_{\mathrm{DES}}$ is a scalar constant ($C_{\mathrm{DES}} = 0.65$). As demonstrated by Spalart *et al.*,[61] starting from the distance $C_{\mathrm{DES}}\Delta$, where the production and destruction terms for $\tilde{\nu}$ (the last two terms in Eq. (3), respectively) balance each other, the eddy viscosity is adjusted to scale with the local deformation rate $\mathscr{S} = 2\sqrt{\mathscr{S}_{ij}\mathscr{S}_{ij}}$ ($\mathscr{S}_{ij}$ is the rate-of-strain tensor of the velocity field) and the distance $\tilde{d}$, i.e., $\tilde{\nu} \propto \mathscr{S}\tilde{d}$. Therefore, close to the wall (i.e., where $d \ll C_{\mathrm{DES}}\Delta$) the model is equivalent to the classical Spalart–Allmaras one (i.e., it behaves like a RANS model). In contrast, far from the wall (i.e., where $d \gg C_{\mathrm{DES}}\Delta$) the model reduces to $\tilde{\nu} \propto \mathscr{S}\Delta$, i.e., it is equivalent to the Smagorinsky one,[62] which scales the sub-grid scale eddy viscosity with the strain rate $\mathscr{S}$ and the size of the filter, $\Delta$, which is tied to the resolution of the computational grid.

For the numerical solution of the governing Eqs. (1) and (3), an in-house, finite-volume solver has been adopted.[57,58,63] The discretization of the computational domain was based on an overlapping grids strategy.[64,65] The numerical approximation of the convective fluxes was obtained by a fourth-order centered formula, whereas the viscous fluxes were estimated by a standard second-order scheme. More details about the discretization in space can be found in our earlier works.[57,58,63]

Pressure-velocity coupling was achieved through a pseudo-compressibility approach.[66] The advancement of the solution in the physical time was carried out by means of a second-order, three-points implicit backward finite-difference discretization. The discretization in the pseudo-time was based on the Euler implicit scheme. A local time-stepping approach and a multigrid method[67] were adopted to accelerate the convergence toward a steady-state solution in the pseudo-time, which is a divergence-free solution in the physical time. In particular, in the present study four grid levels were utilized: at each level the grid size was doubled in each direction, compared to the higher level grid. Therefore, at the second, third, and fourth grid levels the cells number was diminished of factors 8, 64, and 512, relative to the finest, first-level grid.

## III. SETUP

DES computations were conducted on the rotor of an axial-flow, hydrokinetic turbine for five values of $\lambda = \hat{\Omega}\hat{R}/\hat{U}_\infty$, where $\hat{\Omega}$ is the rotational speed of the turbine, $\hat{R}$ the radial extent of its rotor and $\hat{U}_\infty$ the axial velocity of the incoming flow. All non-dimensional quantities below are scaled by $\hat{D}$, $\hat{U}_\infty$ and $\hat{\rho}$, unless otherwise stated, where $\hat{D}$ is the diameter of the rotor and $\hat{\rho}$ is the density of the fluid. The simulated values of $\lambda$ are reported in Table I, where also both the diameter and chord-based Reynolds numbers, $Re_D$ and $Re_c$, are provided. They are defined, respectively, as $Re_D = \hat{D}\hat{U}_\infty/\hat{\nu}$ and $Re_c = \hat{c}\hat{W}/\hat{\nu}$, where $\hat{c}$ is the chord of the rotor blades at 75%$\hat{R}$ from the axis of the rotor and $\hat{W}$ is the magnitude of the relative velocity of the incoming flow at the same radial location, computed as $\hat{W} = \sqrt{\hat{U}_\infty^2 + (0.75\hat{R}\hat{\Omega})^2}$. It should be observed that $\lambda$ was changed across cases by varying the rotational speed. Therefore, as shown in Table I, $Re_D$ is constant, while $Re_c$ is variable across values of $\lambda$.

The geometry of the rotor is illustrated in Fig. 1. Its blades are the same as in the hydrokinetic (tidal) turbine model considered in the physical experiments by Draycott *et al.*,[68] who conducted measurements in the FloWave Ocean Energy Research Facility at the University of Edinburgh, across a wide range of values of $\lambda$, including the ones reported in Table I. The model-scale Reynolds numbers are the same as those we simulated. Our numerical model considered a simplified geometry of the hub and no supporting tower downstream of the rotor. The absence of the support in the numerical model

**TABLE I.** Simulated working conditions.

| $\lambda$ | $Re_D$ | $Re_c$ |
|---|---|---|
| 4.00 | $1.04 \times 10^6$ | $1.51 \times 10^5$ |
| 5.00 | $1.04 \times 10^6$ | $1.85 \times 10^5$ |
| 6.45 | $1.04 \times 10^6$ | $2.35 \times 10^5$ |
| 8.00 | $1.04 \times 10^6$ | $2.90 \times 10^5$ |
| 10.00 | $1.04 \times 10^6$ | $3.60 \times 10^5$ |

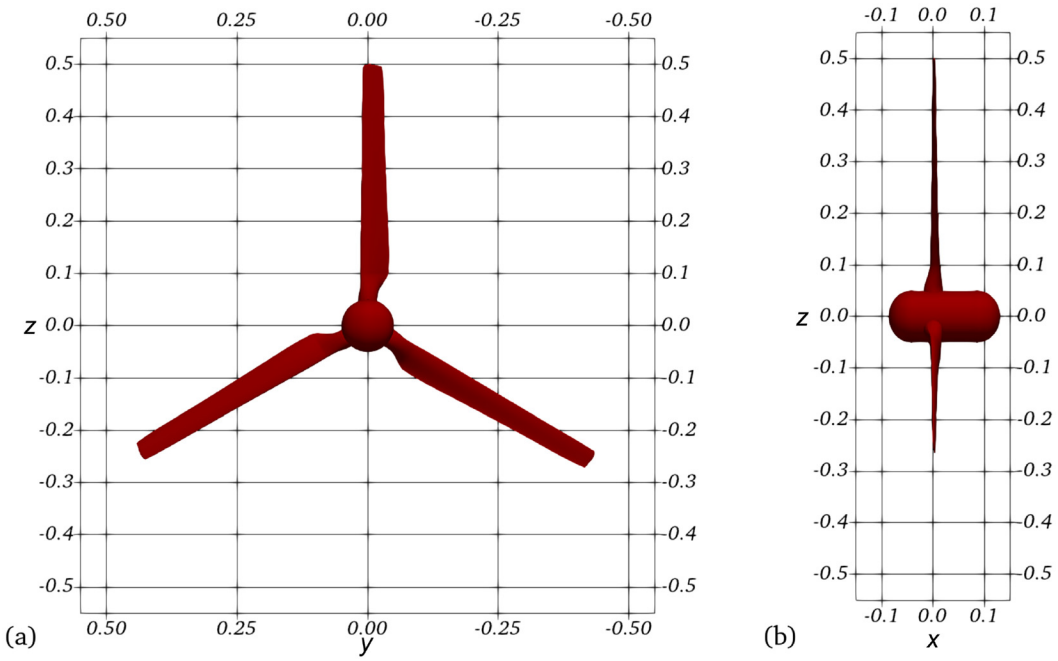


**FIG. 1.** Geometry of the rotor: (a) frontal view and (b) side view.

allowed us to simulate the flow in a reference frame rotating with the turbine, resulting in a dramatic speed-up of the computations and saving of core-hours.

All computations were conducted using an overlapping grids strategy. The computational domain was discretized by a cylindrical, background grid, using additional refinement blocks around the turbine and in its wake. Blocks with both Cartesian and toroidal topologies were adopted, with the purpose of increasing the resolution in the regions where sharp gradients are expected, as in the areas populated by the tip and hub vortices. A visualization of a meridian section of the grid blocks in the vicinity of the rotor and in its near wake is provided in Fig. 2. Details of the blocks discretizing the region of space around the blades are visualized in Fig. 3.

The grid was designed to achieve an average near wall spacing below one viscous length, so no wall-functions were required, since the boundary layer over the surface of the bodies immersed within the flow was resolved. Details on the grid resolution in wall-units, $y^+$, over the surface of the blades are given in Fig. 4, where panels (a) and (b) deal with the pressure and suction sides, respectively. A decrease in the values of $y^+$ occurs at the tip of the blade, thanks to the refinement blocks designed to resolve that region. Figure 4(c) provides also the number of grid cells over the surface of each blade within each particular range of wall resolution. About the resolution in the near wake, it was designed to properly resolve the tip vortices. For instance, at one diameter downstream of the plane of the turbine the size of the grid cells resolving those structures was equivalent to about $4.0 \times 10^{-3}D$, $5.5 \times 10^{-3}D$ and $1.0 \times 10^{-2}D$ along the streamwise, radial, and azimuthal directions, respectively. As discussed below, defining the tip vortices as the region where $Q > 15$ ($Q$ is the second invariant of the velocity gradient tensor), this resolution was

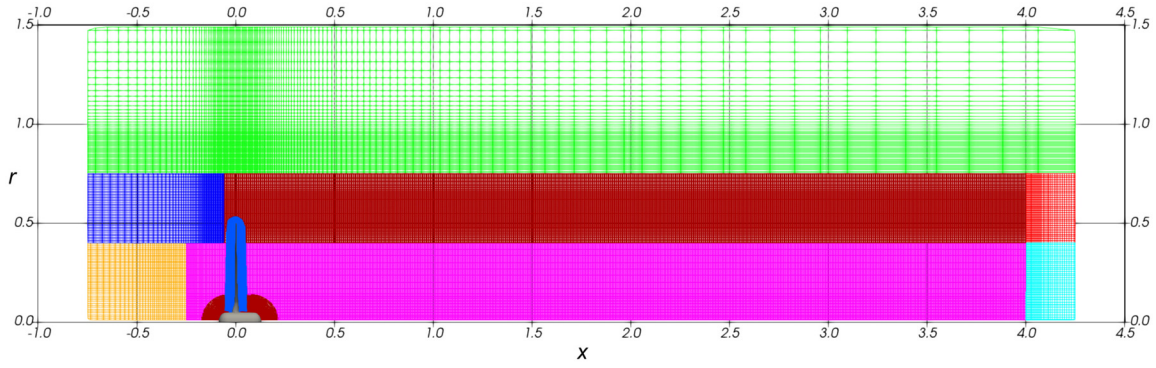


**FIG. 2.** Detail of a meridian section of the mesh, showing the overlapping grids in the region in the vicinity of the rotor.

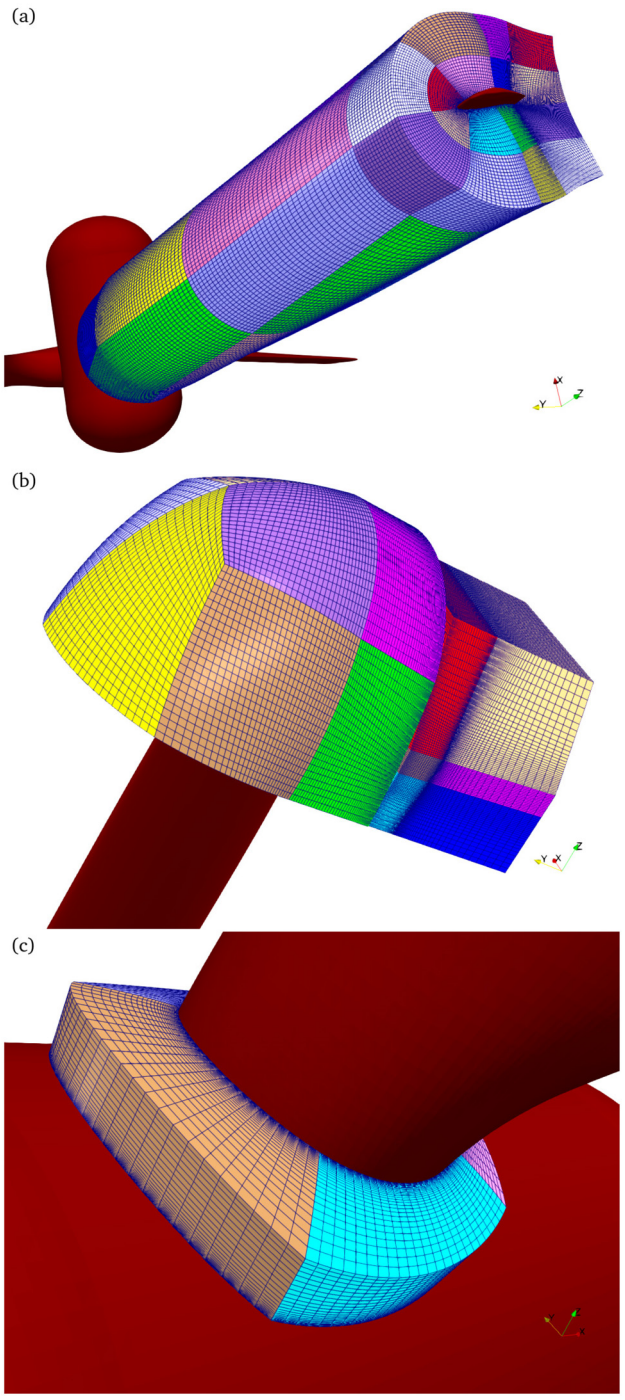


**FIG. 3.** Blocks of the mesh discretizing the regions (a) across the span of each blade, (b) its tip, and (c) its root.

equivalent to about 20 cells across the diameter of the cross section of the tip vortices.

An in-house, overlapping grid preprocessor[65] was utilized to assemble the overall grid. In total, the grid was composed of 288 blocks

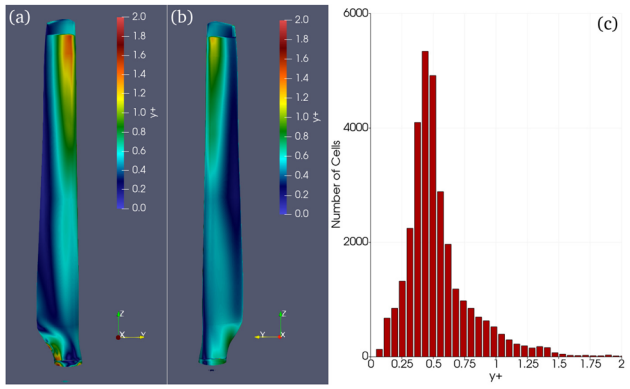


**FIG. 4.** Resolution of the computational grid in wall-units: (a) pressure side of a blade, (b) suction side of a blade, and (c) number of grid cells over the blade within each range of near wall resolution.

for the near field discretization (i.e., the blades of the rotor and the nacelle) and 19 blocks to resolve the wake and the far field, for a total of about $35.7 \times 10^6$ finite volumes: about $10.1 \times 10^6$ of them were utilized for the solution of the flow within the region of the body-fitted grid around the rotor (the hub and the three blades), about $22.8 \times 10^6$ for the solution of the wake flow and about $2.8 \times 10^6$ for the far field. Details are provided in Table II.

Computations were carried out enforcing a constant time step: the resolution in time was equivalent to a rotation of 1° per time step. The size of the domain ranged from six diameters upstream of the rotor plane to ten diameters downstream. The lateral boundaries were placed at ten diameters from the axis of the cylindrical domain. Dirichlet, uniform boundary conditions were adopted for velocity at the inflow and for pressure at the outflow. In particular, a uniform axial velocity was prescribed at the inlet section of the domain. Homogeneous Neumann conditions were enforced for pressure at the inlet and for the velocity vector at the outlet. Free-stream conditions were prescribed at the lateral boundary of the computational domain, i.e., a homogeneous Neumann condition was enforced for all variables. No-slip conditions for velocity and zero pressure gradient along the normal direction were enforced on the surface of the rotor.

All simulations were advanced in time for at least two flow-through times to develop the solution and achieve statistically steady conditions. Then, statistics were computed across ten revolutions. Computations were performed on high-performance computing clusters. Coarse grain (distributed memory) and fine grain (shared memory) parallelizations were achieved via calls to standard Message

**TABLE II.** Mesh details.

| Zone | Number of blocks | Number of cells |
|---|---|---|
| Hub | 18 | 1.7 M |
| Blade root (each) | 4 | 0.1 M |
| Blade (each) | 64 | 1.5 M |
| Blade tip (each) | 22 | 1.2 M |
| Far field | 7 | 2.8 M |
| Wake refinement blocks | 12 | 22.8 M |

Passing Interface and Open Message Passing libraries. In the present study, each case utilized 192 cores, resulting in a computational cost of about 250 000 core hours.

## IV. RESULTS

In the following, the radial, azimuthal, and axial coordinates are denoted as $r$, $\vartheta$, and $x$, respectively. The origin of the radial coordinate, which is oriented outwards, is placed on the rotor axis. The axial coordinate is oriented downstream and its origin is on the plane through the mid chord of the blades at the radial coordinate $75\%\hat{R}$ (note that the streamwise location of the mid chord is a function of the radial coordinate).

The power and thrust coefficients are defined as

$$C_P = \frac{\hat{P}}{\frac{1}{2}\hat{\rho}\hat{A}\hat{U}_\infty^3}, \quad C_T = \frac{\hat{T}}{\frac{1}{2}\hat{\rho}\hat{A}\hat{U}_\infty^2}, \tag{6}$$

where $\hat{P}$ is the power extracted by the rotor from the flow, $\hat{T}$ is the axial force experienced by the rotor, and $\hat{A} = \pi\hat{D}^2/4$ is the frontal area of the rotor.

Below, the non-dimensional radial, azimuthal, and axial velocity components are denoted as $u_r$, $u_\vartheta$, and $u_x$, respectively, while the non-dimensional pressure is indicated as $p$. In the following discussion of the results, both time-averaged and phase-averaged statistics are presented. The former are computed in an inertial reference frame, where the observer sees the blades rotating, while the latter are computed in a reference frame rotating together with the rotor, where the blades are stationary, relative to the observer. The operators $\overline{\cdot}$ and $\langle\cdot\rangle$ are utilized to denote time-averaged and phase-averaged statistics, respectively. The fluctuations in time are indicated as $\cdot'$.

The turbulent kinetic energy is defined as

$$\overline{k} = \frac{1}{2}\left[\overline{(u_r')^2} + \overline{(u_\vartheta')^2} + \overline{(u_x')^2}\right], \tag{7}$$

where $\overline{(u_r')^2}$, $\overline{(u_\vartheta')^2}$, and $\overline{(u_x')^2}$ are the time-averaged mean-squares of the fluctuations of radial, azimuthal and axial velocity components, respectively. The phase-averaged turbulent kinetic energy is based on a similar definition, considering instead the phase-averaged mean-squares of the fluctuations of the three velocity components.

The analysis of the results of the computations is organized as follows. In the Sec. IV A, verification and validation are reported on the global parameters of performance of the rotor. Then, Sec. IV B provides an overview of the flow and a glimpse of the phenomena of mutual inductance, pairing, and instability of the vortices shed from the tip of the blades. The following Sec. IV C illustrates these phenomena in detail, showing the strong dependence of their streamwise coordinate on the value of the tip speed ratio. The velocity spectra of Sec. IV D give additional evidence of this dependence, characterized by a shift of the leading frequency in the wake of the rotor from the blade frequency to the shaft frequency, as the pairing events between tip vortices lead to the onset of a single helical vortex, eventually experiencing auto-inductance phenomena and the resulting instability. This instability is the source of increasing levels of turbulent stresses, especially at the outer boundary of the wake, as demonstrated in Sec. IV E. The breakup of the tip vortices starts the process of recovery of streamwise momentum in the wake core of the turbine, as discussed in the Sec. IV F as a function of the tip speed ratio. The Sec. IV G shows that this recovery is mainly tied to phenomena of radial advection, resulting from the onset of inward radial flows from the free stream into the wake core.

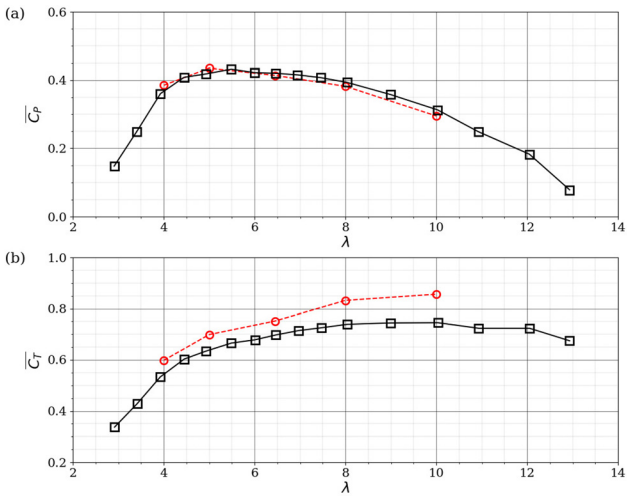


**FIG. 5.** Comparison between the present computations (circles) and the measurements by Draycott *et al.*[68] (squares) on the time-averaged power (a) and thrust (b) coefficients.

**TABLE III.** Verification assessment for power and thrust coefficients.

| $\lambda$ | Load | $S_3$ | $S_2$ | $S_1$ | $\mathscr{P}$ | Convergence | $S_{RE}$ | $\frac{U_{FSM}}{S_1}$ |
|---|---|---|---|---|---|---|---|---|
| 4.00 | $\overline{C}_P$ | 0.346 | 0.378 | 0.385 | 2.18 | MC | 0.387 | 1.62% |
| | $\overline{C}_T$ | 0.523 | 0.584 | 0.598 | 2.07 | MC | 0.603 | 1.57% |
| 5.00 | $\overline{C}_P$ | 0.361 | 0.413 | 0.426 | 1.97 | MC | 0.431 | 1.67% |
| | $\overline{C}_T$ | 0.624 | 0.685 | 0.699 | 2.17 | MC | 0.703 | 1.71% |
| 6.45 | $\overline{C}_P$ | 0.376 | 0.405 | 0.414 | 1.79 | MC | 0.417 | 1.21% |
| | $\overline{C}_T$ | 0.690 | 0.739 | 0.752 | 1.82 | MC | 0.758 | 1.38% |
| 8.00 | $\overline{C}_P$ | 0.351 | 0.419 | 0.382 | ··· | OC | ··· | ··· |
| | $\overline{C}_T$ | 0.778 | 0.874 | 0.832 | ··· | OC | ··· | ··· |
| 10.00 | $\overline{C}_P$ | 0.288 | 0.327 | 0.295 | ··· | OC | ··· | ··· |
| | $\overline{C}_T$ | 0.835 | 0.917 | 0.855 | ··· | OC | ··· | ··· |

**TABLE IV.** Validation assessment for power and thrust coefficients.

| $\lambda$ | Load | EXP | DES | $\frac{\varepsilon}{\text{EXP}}$ |
|---|---|---|---|---|
| 4.00 | $\overline{C}_P$ | 0.367 | 0.387 | 5.40% |
| | $\overline{C}_T$ | 0.543 | 0.603 | 11.01% |
| 5.00 | $\overline{C}_P$ | 0.420 | 0.431 | 2.51% |
| | $\overline{C}_T$ | 0.638 | 0.703 | 10.11% |
| 6.45 | $\overline{C}_P$ | 0.420 | 0.417 | −0.79% |
| | $\overline{C}_T$ | 0.697 | 0.758 | 8.74% |
| 8.00 | $\overline{C}_P$ | 0.394 | 0.382 | −3.17% |
| | $\overline{C}_T$ | 0.738 | 0.832 | 12.76% |
| 10.00 | $\overline{C}_P$ | 0.314 | 0.295 | −6.16% |
| | $\overline{C}_T$ | 0.746 | 0.855 | 14.72% |

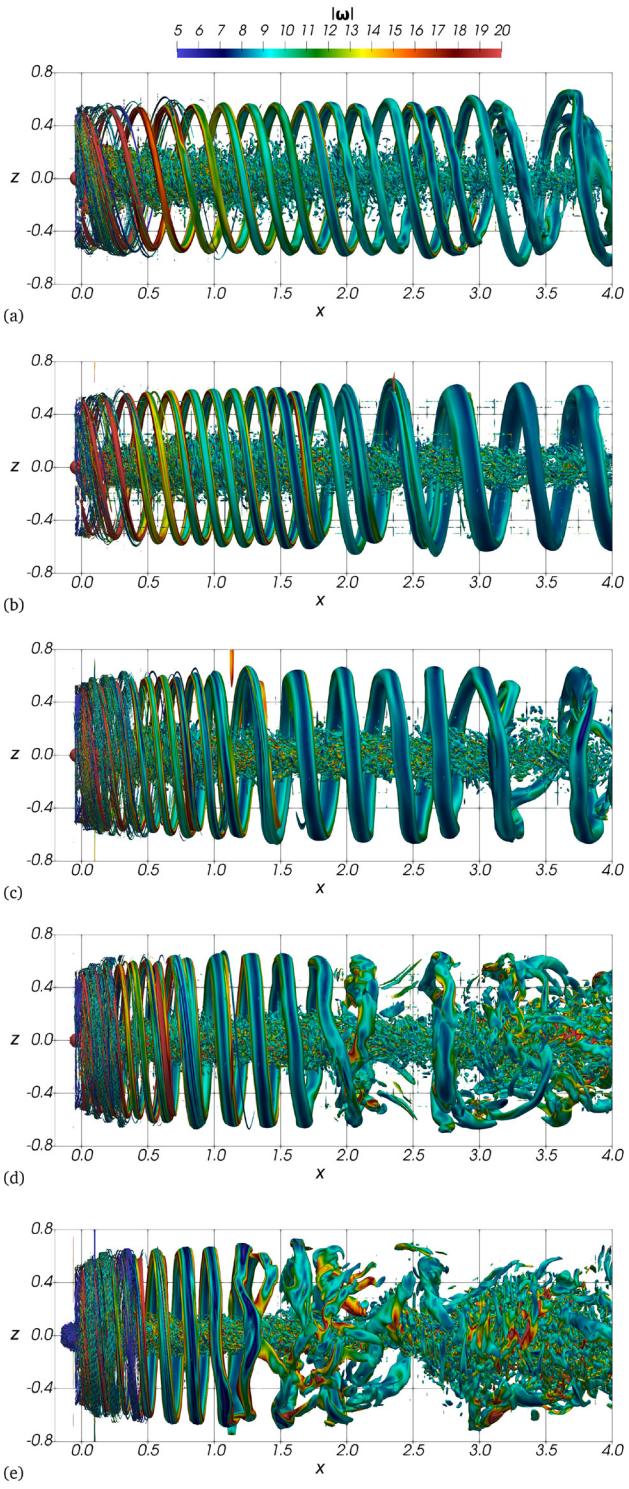


**FIG. 6.** Visualization of the tip vortices by means of isosurfaces of the second invariant of the velocity gradient tensor[70,71] ($Q = 15$) from instantaneous realizations of the solution for (a) $\lambda = 4.00$, (b) $\lambda = 5.00$, (c) $\lambda = 6.45$, (d) $\lambda = 8.00$, and (e) $\lambda = 10.0$, colored by the vorticity magnitude.

### A. Verification and validation

Comprehensive verification (i.e., the assessment of the order of convergence and numerical uncertainty) and validation (i.e., the comparison against reference data) of the results from DES computations are reported for the time-averaged power and thrust coefficients.

Verification is conducted following the so-called *factor of safety method* (FSM).[69] Numerical results for different grid refinements are obtained by exploiting the multigrid capabilities of the solver, i.e., the numerical solutions are computed on the three finest grid levels, generated by removing from the next finer one every other grid points. Accordingly, the time steps on the coarser grid levels are also recursively doubled. The results of the verification assessment are summarized in Table III.

In Table III, $S_3$, $S_2$, and $S_1$, denote the results from the coarse, medium and fine meshes, consisting of 0.6, 4.5, and $35.7 \times 10^6$ cells, respectively, whereas the estimated order of accuracy is indicated as $\mathscr{P}$. In order to compare the uncertainty with the estimated solution, the numerical uncertainties at 95% confidence level ($U_{\mathrm{FSM}}$) on the power and thrust coefficients are reported for the finest grid as percentage of the relevant solution, $S_1$. Since a negligible iterative uncertainty was verified (of the order of 0.01% of the solution), the grid uncertainty can be considered as the only significant contribution to the numerical uncertainty. The type of convergence is also reported in Table III: MC and OC denote monotonic and oscillatory convergence, respectively. Following the FSM, the numerical uncertainty can be estimated only in the case of monotonic convergence.

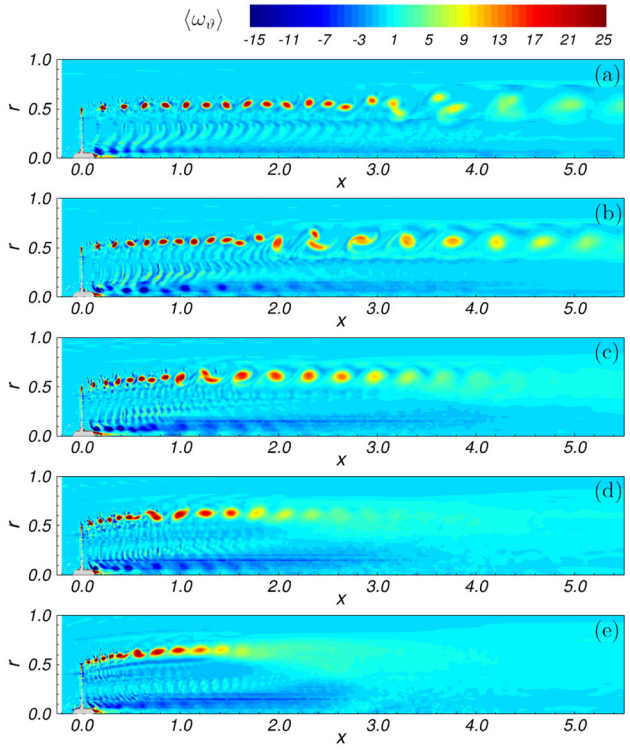


**FIG. 7.** Phase-averaged contours of azimuthal vorticity for (a) $\lambda = 4.00$, (b) $\lambda = 5.00$, (c) $\lambda = 6.45$, (d) $\lambda = 8.00$, and (e) $\lambda = 10.0$.

The results in Table III show monotonic convergence for the lowest values of $\lambda$, characterized by an actual order of convergence close to the theoretical value, that is 2, for both power and thrust coefficients. Instead, oscillatory convergence is observed for the highest values of $\lambda$. The numerical uncertainty is always less than 2% of $S_{RE}$ for the lowest values of $\lambda$, which are those characterized by monotonic convergence.

The time-averaged results on the parameters of performance are compared against the experiments by Draycott *et al.*[68] Tests were carried out at the same values of $Re$ and $\lambda$ as the present computations (Table I), keeping a constant value of the free-stream velocity equal to 0.866 m/s and changing the rotational speed of the turbine for testing different values of $\lambda$. Draycott *et al.*[68] utilized a turbine model with a rotor of diameter $\hat{D} = 1.2$ m and blades of chord length $\hat{c} = 55$ mm at 75%$\hat{R}$.

The comparison between experiments (EXP) and DES results is shown in Fig. 5 and in Table IV. The largest differences between DES and EXP, $\varepsilon$, are observed for the largest and smallest values of $\lambda$, i.e., when the turbine is working far away from the design condition. In the other cases the relative error ($\varepsilon$/EXP) on the power coefficient is within 4%. On average, the thrust is overestimated by DES by about 11%, compared to the measurements. Taken into account the agreement on the power coefficient, the likely reason for the difference affecting the thrust coefficient is attributable to the vertical support downstream of the rotor, utilized during the experiments, but missing in the computational model. This generates a blockage downstream of the turbine, increasing the pressure levels on the suction side of its blades and reducing the average axial force experienced by its rotor. This blockage is missing in the computations, resulting in a more significant jump of pressure between the upstream, pressure side of the blades and their downstream, suction side.

### B. Overview of the flow

Figure 6 provides an overview of the influence of $\lambda$ on the wake features. Increasing rotational speeds result in a faster development of the instability of the tip vortices. They deviate from their initial helical trajectory, undergo coupling, and eventually lose their coherence, breaking up into smaller structures. The speed of this process increases with $\lambda$. It is known that the helical trajectory of the tip vortices is subject to both short-wave and long-wave instabilities.[72] These deviations of the tip vortices from their theoretical trajectories trigger mutual inductance phenomena, which amplify vortex meandering and promote coupling between them. Higher values of $\lambda$ result into a smaller pitch of the tip vortices, i.e., a smaller angle relative to the azimuthal direction and a shorter distance between the spirals of the tip vortices. As a result, for increasing values of $\lambda$ their mutual inductance is accelerated and so is the resulting breakup of their coherence, in agreement

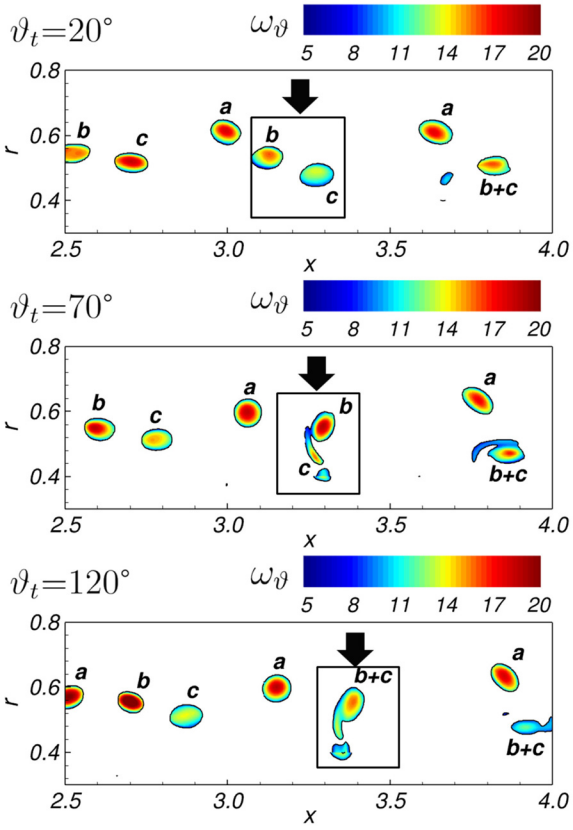


**FIG. 8.** Instantaneous realizations of the solution for $\lambda = 4.00$. Contours of azimuthal vorticity in the areas of $Q > 15$. Arrows indicating the first pairing event between tip vortices.

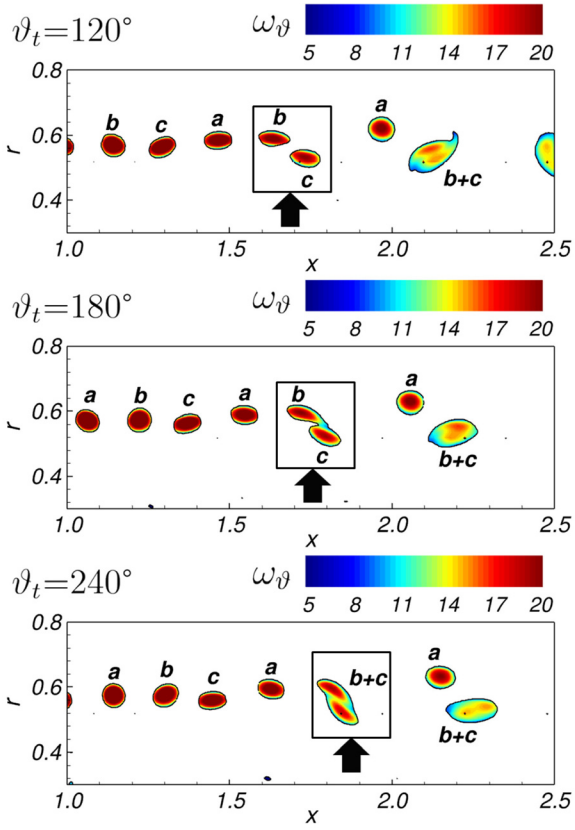


**FIG. 9.** Instantaneous realizations of the solution for $\lambda = 5.00$. Contours of azimuthal vorticity in the areas of $Q > 15$. Arrows indicating the first pairing event between tip vortices.

with the behavior observed in the wake of marine propellers.[56,73–77] Interestingly, the results in Fig. 6 show that first the tip vortices experience mutual inductance, leading them to join into a single, larger helical vortex. Then, this vortex undergoes auto-inductance, which leads to instabilities, vortex meandering and eventual breakdown. This result indicates that the theoretical studies on isolated helical vortices[72,78–80] are also relevant to the dynamics of the wake of actual turbines, although consisting of multiple blades shedding multiple tip vortices, since the later stages of the instability process are governed by auto-inductance phenomena.

Figure 7 shows contours of phase-averaged azimuthal vorticity. By providing the signature of the tip vortices on the plane, they highlight the decreasing distance between tip vortices at higher values of $\lambda$. Meanwhile, they show the wider signature of the vortex originating from the pairing of the original helical vortices. However, as $\lambda$ grows, the signature of this vortex diffuses at more upstream locations, as a result of its earlier breakdown. In Sec. IV F, we will demonstrate the influence of this phenomenon on the speed of wake recovery.

### C. Coupling process of the tip vortices

The visualizations in Sec. IV B pointed out phenomena of paring of the tip vortices. This phenomenon is clearly visible on an azimuthal plane cutting the tip helical vortices, as in the instantaneous snapshots reported in this section (Figs. 8–19). The traces of the helical tip vortices on the plane are equally spaced when formed, but as they advect downstream, two vortices are attracted to each other, resulting in a pair of co-rotating vortices, until they merge into one single helical vortex. Eventually, auto-inductance phenomena involving the spirals of this single vortex accelerate its process of instability. This sequence of events leads to the breakup of the coherence of the tip vortices shed by the rotor and is faster at higher values of $\lambda$. In this section, this phenomenon is discussed in detail for each $\lambda$. In agreement with the visualizations of Fig. 6, this process is discussed up to $x/D = 4.0$, where the grid resolution is fine enough to avoid numerical diffusion of the coherent structures.

The $\lambda = 4.00$ case is illustrated in Fig. 8, where contours of azimuthal vorticity are visualized in the regions where $Q > 15$ ($Q$-criterion by Jeong and Hussain[71]) with the purpose of isolating the core of the tip vortices. A sequence of three instantaneous realizations of the solution is provided, corresponding to a rotation of 50° between panels, where $\vartheta_t$ represents the angular position of the turbine, relative to that visualized in Fig. 1. It is worth noting that for this small value of $\lambda$ the extent of the high-resolution block of the computational grid is able to include only the first pairing event between two of the three tip vortices of the wake system. This pairing, involving the tip vortices denoted as $b$ and $c$, is indicated by arrows in Fig. 8 and leads to the

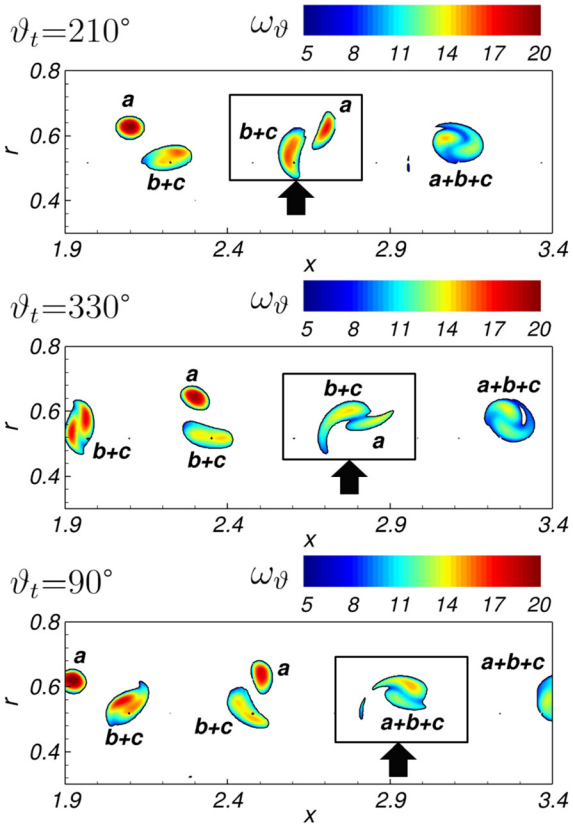


FIG. 10. Instantaneous realizations of the solution for $\lambda = 5.00$. Contours of azimuthal vorticity in the areas of $Q > 15$. Arrows indicating the second pairing event between tip vortices.

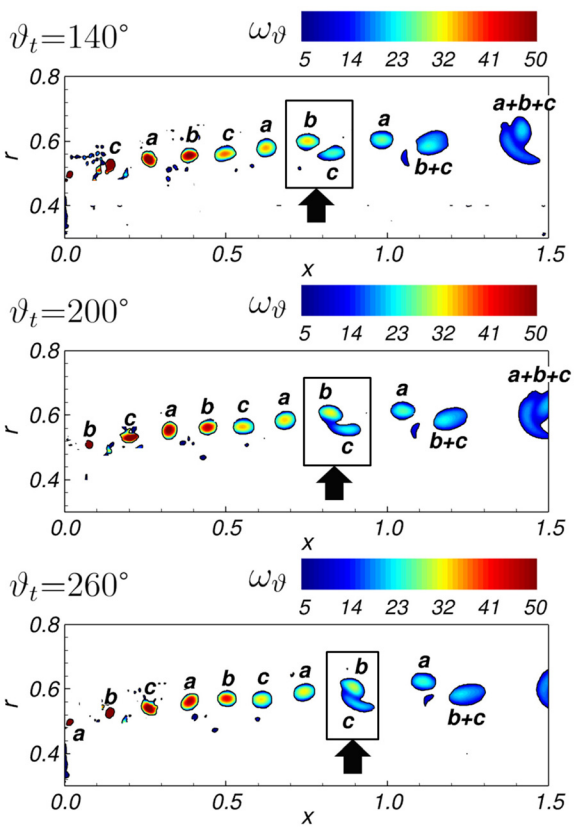


FIG. 11. Instantaneous realizations of the solution for $\lambda = 6.45$. Contours of azimuthal vorticity in the areas of $Q > 15$. Arrows indicating the first pairing event between tip vortices.

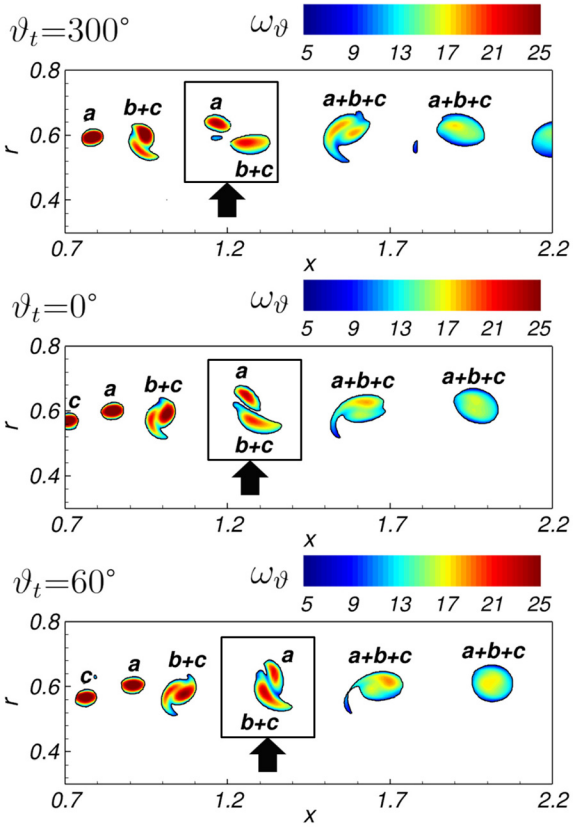


**FIG. 12.** Instantaneous realizations of the solution for $\lambda = 6.45$. Contours of azimuthal vorticity in the areas of $Q > 15$. Arrows indicating the second pairing event between tip vortices.

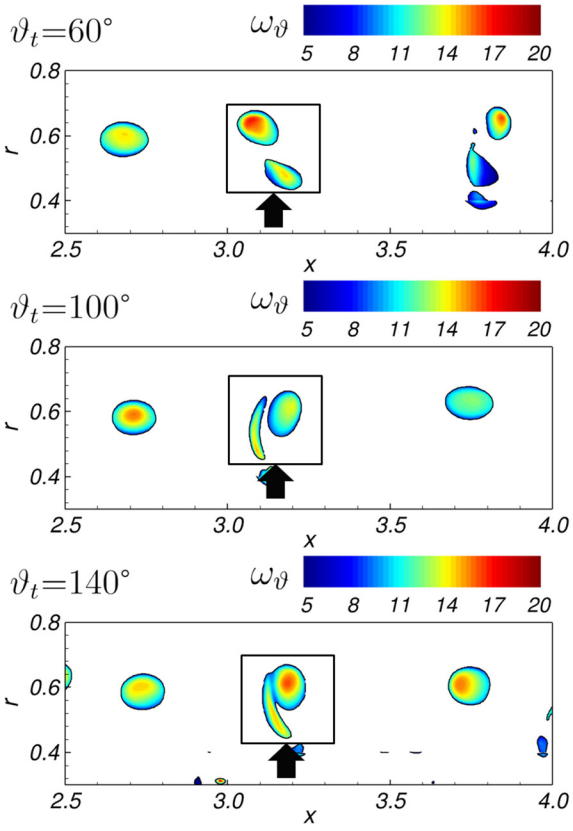


**FIG. 13.** Instantaneous realizations of the solution for $\lambda = 6.45$. Contours of azimuthal vorticity in the areas of $Q > 15$. Arrows indicating an auto-inductance event between spirals of the single helical vortex originated more upstream from the three vortices shed by the rotor.

formation of a larger vortex, denoted as $b + c$. As shown in Fig. 6(a), at $x/D = 4.0$ the two vortices composing the wake system after this pairing event, which are indicated as $a$ and $b + c$ in Fig. 8, are still separated and coherent.

Figure 9 shows the first coupling for $\lambda = 5.00$, occurring at about $x/D \approx 1.8$. This is faster than that seen in Fig. 8, which is located at about $x/D \approx 3.3$. For this higher value of $\lambda$, the streamwise extent of the finer region of the computational grid is large enough to capture also the second pairing, leading to a system consisting of a single helical vortex. This is illustrated in the sequence of Fig. 10, where the two remaining vortices join into a single vortex at about $x/D \approx 2.9$. As shown in Fig. 6(b), this vortex is still stable and coherent at the outlet boundary of the high-resolution region of the computational grid.

For $\lambda = 6.45$, the first and second coupling events move further upstream, at the streamwise locations $x/D \approx 0.8$ and $x/D \approx 1.3$, respectively. They are illustrated in the visualizations of Figs. 11 and 12. These events lead to a wake system consisting of a single helical vortex, indicated as $a + b + c$ in Fig. 12. For this case of $\lambda$, the stremwise extent of the fine region of the domain is large enough to capture also phenomena of auto-inductance of the single vortex $a + b + c$, leading eventually to its instability and breakup. An auto-inductance event is shown at $x/D \approx 3.2$ in Fig. 13, where consecutive spirals of the same helical vortex interact with each other, promoting meandering and accelerating the process of instability.

Figures 14 and 15 show that the first and the second pairing events for $\lambda = 8.00$ are very close to each other: they locate about at the streamwise coordinates $x/D \approx 0.6$ and $x/D \approx 0.7$, respectively. Also, the auto-inductance phenomena, affecting the vortex originating from the merging process of the original tip vortices, occur earlier, compared to that observed in Fig. 13 for $\lambda = 6.45$. At $\lambda = 8.00$, auto-inductance events begin at $x/D \approx 1.9$, as illustrated in Fig. 16. These trends are confirmed at the highest value of $\lambda$: coupling phenomena move closer to the plane of the rotor and become also much closer to each other as the tip speed ratio grows. At $\lambda = 10.0$ these phenomena occur in the range of streamwise coordinates $0.3 < x/D < 0.5$, as illustrated in Figs. 17 and 18. Further downstream, the first auto-inductance events are observed at $x/D \approx 1.2$, as shown in Fig. 19.

Table V summarizes the streamwise locations of the pairing and auto-inductance events discussed in this section across values of tip speed ratio.

### D. Velocity spectra

Probes were placed at the radial coordinate $r/D = 0.55$ from the rotor axis in its wake. Figure 20 shows the power spectral density, *PSD*,

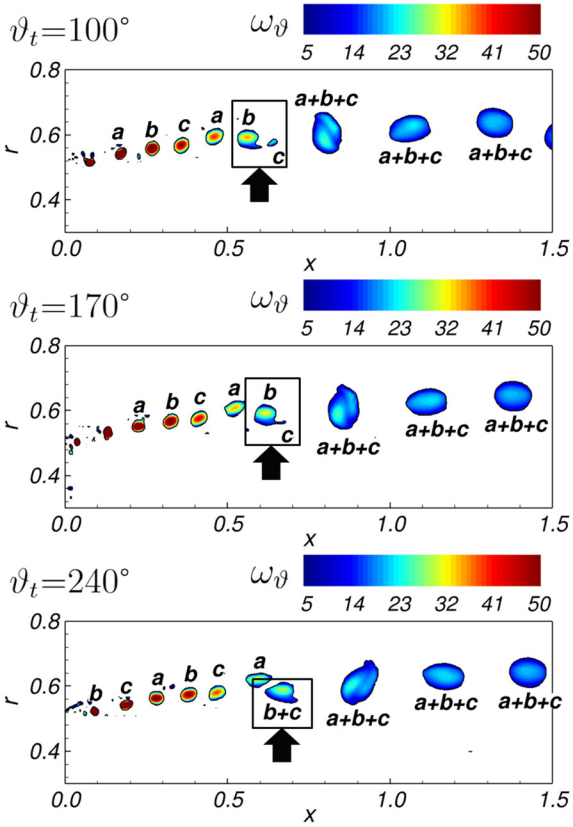


FIG. 14. Instantaneous realizations of the solution for $\lambda = 8.00$. Contours of azimuthal vorticity in the areas of $Q > 15$. Arrows indicating the first pairing event between tip vortices.

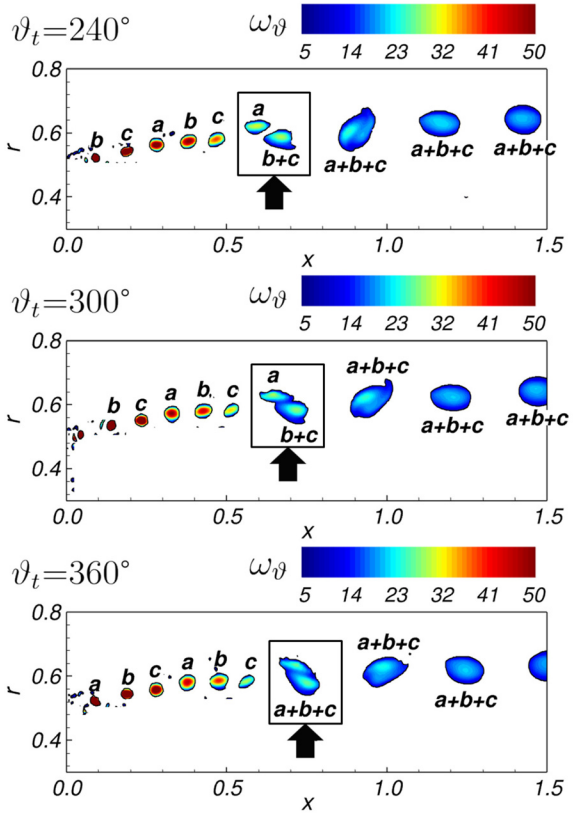


FIG. 15. Instantaneous realizations of the solution for $\lambda = 8.00$. Contours of azimuthal vorticity in the areas of $Q > 15$. Arrows indicating the second pairing event between tip vortices.

of the time history (in a stationary reference frame) of the azimuthal velocity at five streamwise coordinates. Although all probes were placed at the same azimuthal location, this choice does not affect the following results, due to the symmetry of the flow problem. On the horizontal axes, frequencies are scaled using the frequency of the blade passage, $f_b$. Figure 20(a) deals with the lowest value of $\lambda$. This panel displays a strong, leading peak at the frequency $f = f_b$ up to $x/D = 2.0$, due to the passage of the tip vortices shed by the rotor. The maxima at the higher harmonics of $f_b$ are also well distinguishable. Meanwhile, an evident shift of the energy toward lower frequencies is already occurring between $x/D = 0.5$ and $x/D = 2.0$, reinforcing the maxima first at the frequency $f = 2/3f_b$ and then at the frequency $f = 1/3f_b$, indicating that the process of pairing between tip vortices is affecting the distribution of the power spectral density. At $x/D = 3.0$, this shift becomes more obvious: the peak at the blade frequency declines sharply, becoming similar to the maxima corresponding to $f = 1/3f_b$ and $f = 2/3f_b$. This trend is confirmed further downstream, at $x/D = 4.0$, where the peak at $f = 2/3f_b$ becomes smaller, while that at $f = 1/3f_b$ gets even stronger, demonstrating again the transition from a wake system dominated by the blade frequency to one dominated by the shaft frequency, as the coupling between tip vortices results in the onset of a single helical structure. Figure 20(b) deals with the case $\lambda = 5.00$. All phenomena discussed above develop at a faster rate. The blade frequency is the leading one at both $x/D = 0.5$ and $x/D = 1.0$, but already at $x/D = 2.0$ the strongest maxima locate at $f = 1/3f_b$ and $f = 2/3f_b$. In the panels of Figs. 20(c) and 20(d), this change is already distinguishable at $x/D = 1.0$ and $x/D = 0.5$, respectively. Eventually, at the highest tip speed ratio, corresponding to Fig. 20(e), the coupling process is so fast that at $x/D = 0.5$ the peak at the shaft frequency is already orders of magnitude stronger than that at the blade frequency, in line with the visualizations reported above on the influence of $\lambda$ on the streamwise location of the mutual and auto-inductance events.

### E. Development of turbulent stresses

The breakdown of the tip vortices results in increasing levels of turbulent stresses. They are growing functions of both the streamwise coordinate and $\lambda$. This is shown in the phase-averaged contours of Figs. 21 and 22, where the turbulent kinetic energy and the shear stress associated with the resolved fluctuations of the radial and streamwise velocity components are reported. As the instability of the tip vortices develops, both Figs. 21 and 22 show their phase-averaged signature as local maxima/minima of turbulent stresses at the outer boundary of the wake. When their breakup occurs, the signature of the tip vortices is replaced by a wide area of high turbulent stresses, expanding radially

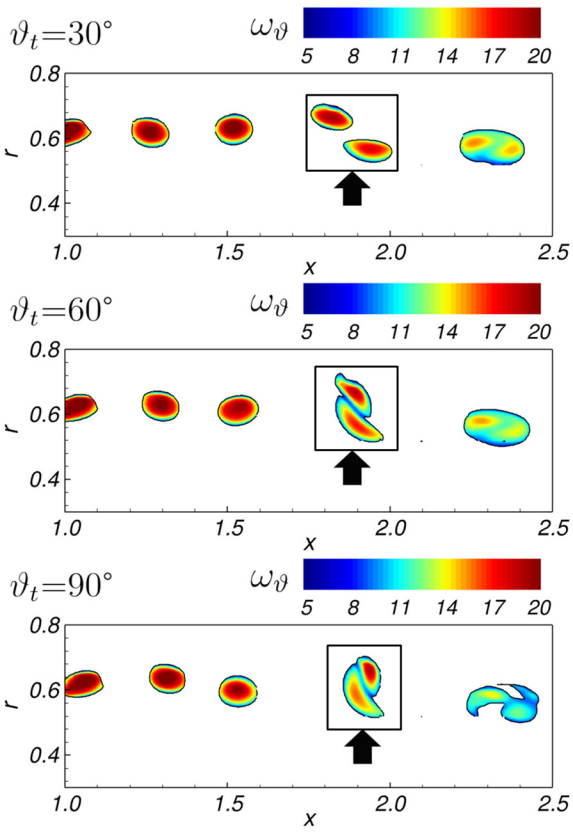


FIG. 16. Instantaneous realizations of the solution for $\lambda = 8.00$. Contours of azimuthal vorticity in the areas of $Q > 15$. Arrows indicating an auto-inductance event between spirals of the single helical vortex originated more upstream from the three vortices shed by the rotor.

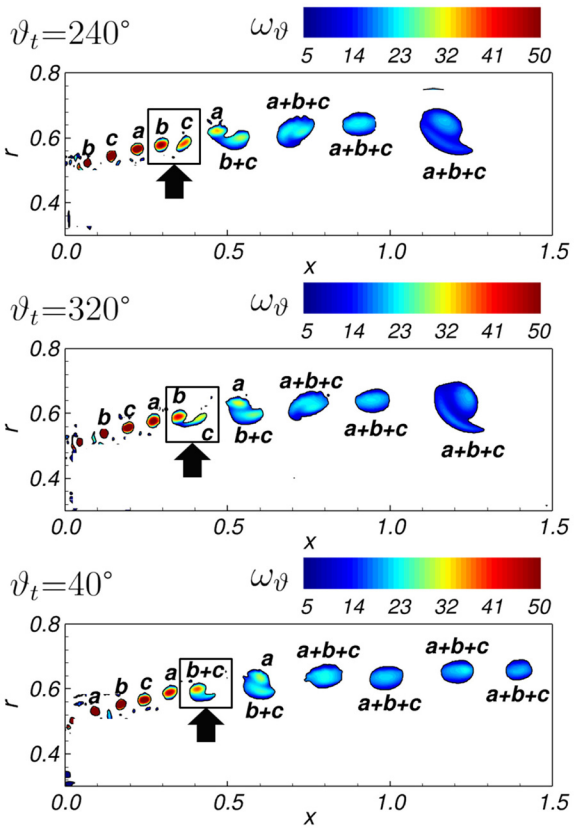


FIG. 17. Instantaneous realizations of the solution for $\lambda = 10.0$. Contours of azimuthal vorticity in the areas of $Q > 15$. Arrows indicating the first pairing event between tip vortices.

toward the wake core for increasing values of $\lambda$. In agreement with our earlier discussion, this area shifts upstream at higher values of $\lambda$. In addition, it becomes wider across both streamwise and radial directions, indicating the growing importance of turbulent mixing for increasing values of $\lambda$. The present results highlight that, although higher values of $\lambda$ produce larger levels of momentum deficit just downstream of the rotor, they trigger a more intense turbulent mixing and in turn a faster wake recovery. These trends are illustrated more quantitatively in Fig. 23. They represent data from the field of turbulent kinetic energy $\overline{k}$, shown in Fig. 24. In Fig. 23, the values of turbulent kinetic energy were averaged over cross sections ranging from the wake axis up to the radial coordinate $R^*$, where the time-averaged streamwise velocity is equivalent to $0.95U_\infty$, which is arbitrarily taken as the outer boundary of the wake. It is shown that the peak intensity of the turbulent stresses grows more than linearly as a function of $\lambda$, besides moving to upstream coordinates.

### F. Speed of wake recovery

The results in Fig. 25 show the streamwise evolution of the time-averaged axial velocity downstream of the rotor, whose wake flow is illustrated by means of time-averaged contours in Fig. 26. At each streamwise coordinate, the streamwise velocity was averaged in space assuming again the wake boundary at the radial location where $\overline{u}_x = 0.95U_\infty$. As expected, the largest momentum deficit just downstream of the turbine is achieved at the highest value of $\lambda$. However, in that case the recovery of the wake starts more upstream and is faster. In Fig. 27, dealing with the streamwise evolution of the radial location of the wake boundary, $R^* = r(\overline{u}_x = 0.95U_\infty)$, although the wake width is initially a growing function of $\lambda$, the case of its highest value is the only one showing wake contraction at downstream coordinates within the available extent of the computational domain, confirming the faster development of the process of wake recovery.

These results are consistent with the discussion reported by Lignarolo *et al.*,[16,17] Posa and Broglia,[13] and Posa *et al.*[15] As long as the tip vortices at the boundary of the wake keep coherent, they act as a "shield" to the penetration of momentum from the free-stream into the wake core. Since at higher values of $\lambda$ their instability is faster, as illustrated in Sec. IV B, also the process of wake recovery is accelerated, despite the achievement of higher levels of momentum deficit just downstream of the rotor. The latter results in stronger radial gradients of streamwise velocity, reinforcing the radial flows developing

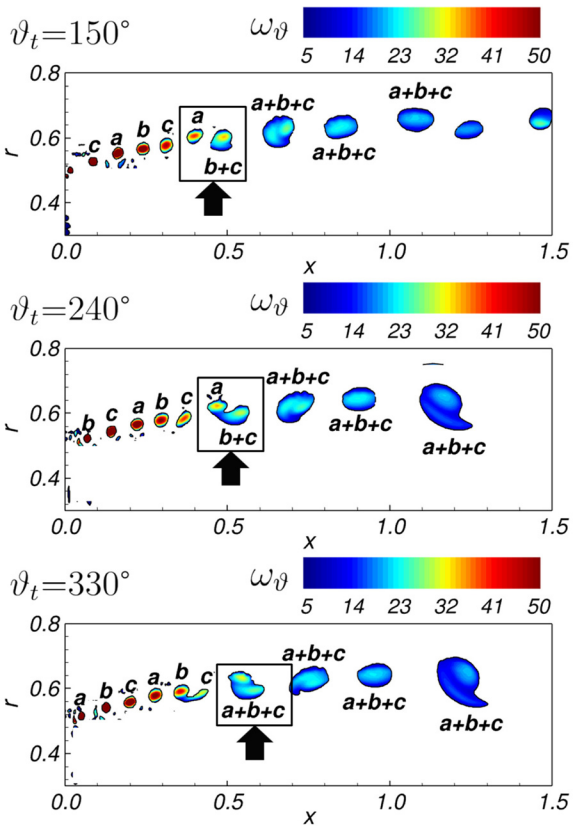


FIG. 18. Instantaneous realizations of the solution for $\lambda = 10.0$. Contours of azimuthal vorticity in the areas of $Q > 15$. Arrows indicating the second pairing event between tip vortices.

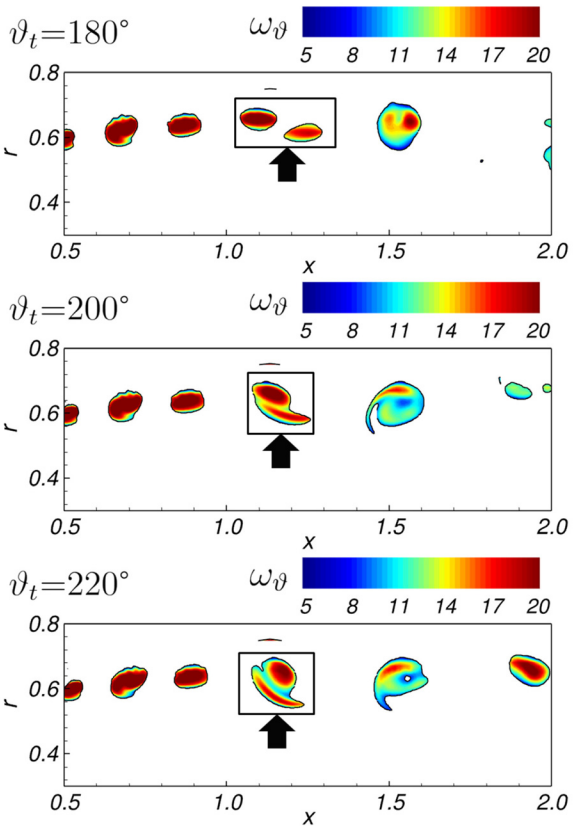


FIG. 19. Instantaneous realizations of the solution for $\lambda = 10.0$. Contours of azimuthal vorticity in the areas of $Q > 15$. Arrows indicating an auto-inductance event between spirals of the single helical vortex originated more upstream from the three vortices shed by the rotor.

downstream of the instability of the tip vortices. In addition, the stronger intensity of the tip vortices at higher loads produces larger values of the turbulent stresses and more intense mixing phenomena when they undergo instability, as discussed in Sec. IV E, promoting further the process of wake recovery at higher tip speed ratios.

### G. Comparisons across terms of wake recovery

To gain more insight into the mechanism of wake recovery, in this section the time-average of the streamwise component of the momentum equation is considered. The streamwise flux of streamwise momentum can be expressed as[35,81–87]

$$\overline{u}_x\frac{\partial \overline{u}_x}{\partial x} = -\overline{u}_r\frac{\partial \overline{u}_x}{\partial r} - \frac{\partial \overline{u_r' u_x'}}{\partial r} - \frac{\partial \overline{u_x' u_x'}}{\partial x} - \frac{\partial \overline{p}}{\partial x} + \frac{1}{Re}\left[\frac{1}{r}\frac{\partial}{\partial r}\left(r\frac{\partial \overline{u}_x}{\partial r}\right) + \frac{\partial^2 \overline{u}_x}{\partial x^2}\right] - \frac{\partial \tau_{jx}}{\partial x_j}, \quad (8)$$

where $\tau_{jx}$ is the $jx$ element of the tensor of the modeled Reynolds stresses. In Fig. 28, the six terms at the right hand side of Eq. (8) are indicated as $\Sigma_i$, with $i = 1, \ldots 6$, where $\Sigma_1$ is the radial advection, $\Sigma_2$ the radial turbulent transport, $\Sigma_3$ the streamwise turbulent transport, $\Sigma_4$ the pressure gradient, $\Sigma_5$ the viscous diffusion, and $\Sigma_6$ the modeled turbulent transport. Positive values of $\Sigma_i$ are equivalent to a positive contribution to replenishment of streamwise momentum downstream of the rotor.

Figure 28(a) shows the most significant contribution to wake recovery, represented by the radial advection of streamwise momentum. Its streamwise evolution was averaged again over cross sections from the wake axis up to the local radial coordinate $R^*$. Radial advection is initially negative, due to wake expansion. This is stronger for increasing values of $\lambda$, due to the growing dynamic solidity of the

TABLE V. Streamwise locations of the pairing and auto-inductance events.

| $\lambda$ | First pairing | Second pairing | Auto-inductance |
|---|---|---|---|
| 4.00 | $x \approx 3.3$ | $x > 4.0$ | $x > 4.0$ |
| 5.00 | $x \approx 1.8$ | $x \approx 2.9$ | $x > 4.0$ |
| 6.45 | $x \approx 0.8$ | $x \approx 1.3$ | $x \approx 3.2$ |
| 8.00 | $x \approx 0.6$ | $x \approx 0.7$ | $x \approx 1.9$ |
| 10.00 | $x \approx 0.4$ | $x \approx 0.5$ | $x \approx 1.2$ |

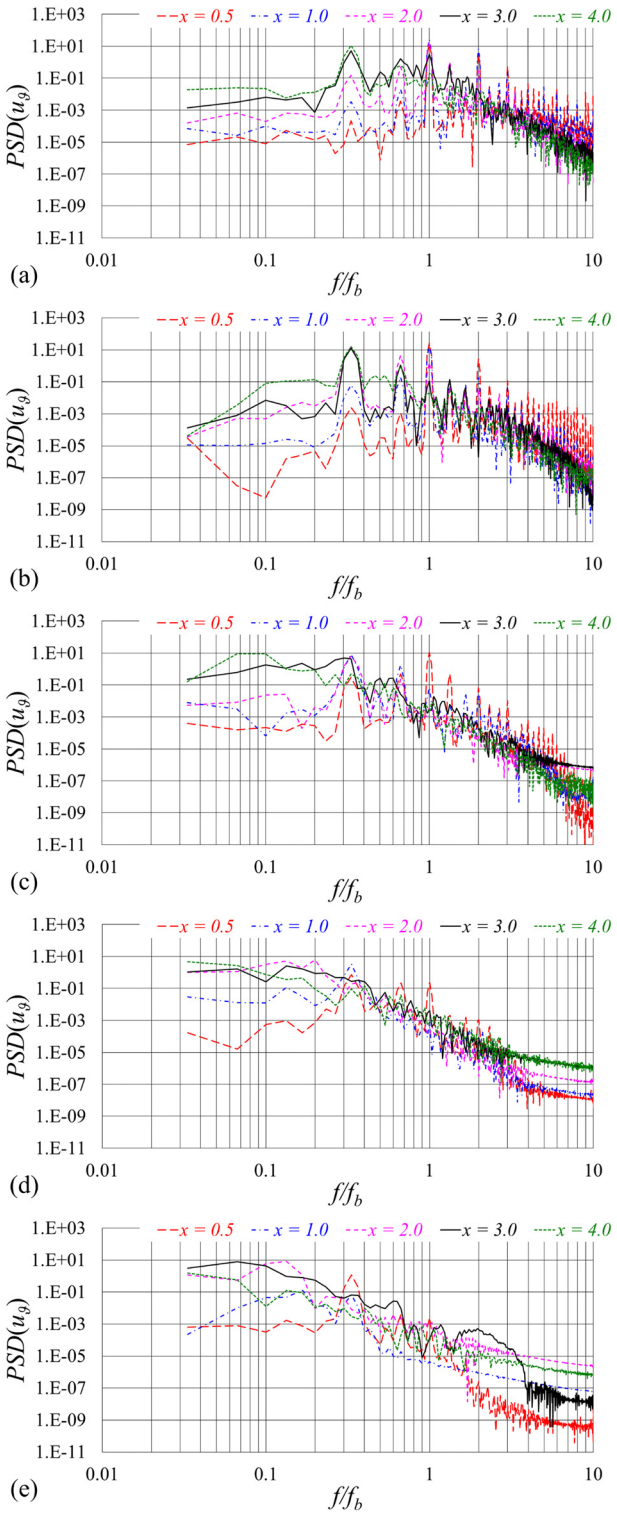


**FIG. 20.** Power spectral density (*PSD*) of the time history of the azimuthal velocity at probes placed at the radial coordinate $r/D = 0.55$: (a) $\lambda = 4.00$, (b) $\lambda = 5.00$, (c) $\lambda = 6.45$, (d) $\lambda = 8.00$, and (e) $\lambda = 10.0$.

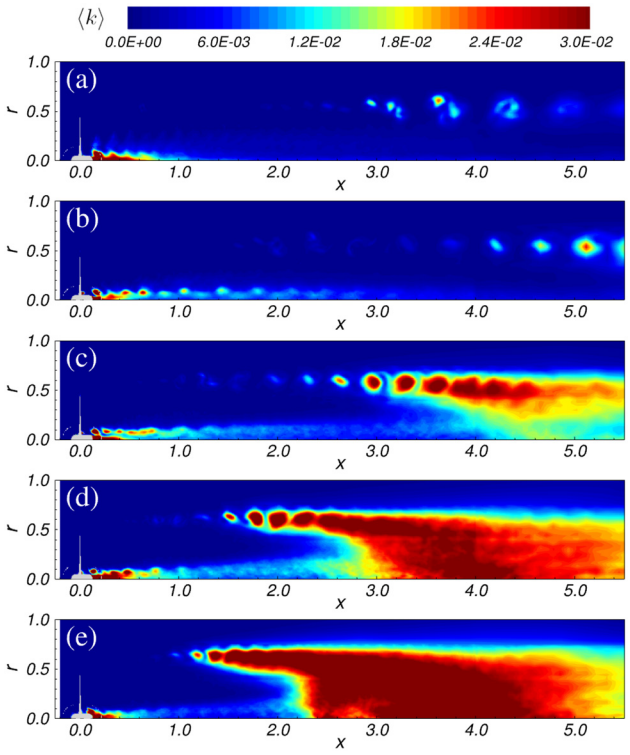


**FIG. 21.** Contours of phase-averaged turbulent kinetic energy on a meridian plane through the axis of the turbine: (a) $\lambda = 4.00$, (b) $\lambda = 5.00$, (c) $\lambda = 6.45$, (d) $\lambda = 8.00$, and (e) $\lambda = 10.0$.

turbine and the resulting larger blockage to the incoming flow. Then, as a result of wake instability, the development of negative, inward radial flows brings streamwise momentum into the wake core from the outer free stream. This phenomenon occurs more upstream and at a faster rate for higher values of $\lambda$, as a result of the faster breakup of the wake coherence. This contribution to wake recovery decays downstream, due to the depletion of the radial gradients of streamwise velocity as the wake gains momentum. This process occurs at a faster rate for increasing values of $\lambda$, due to the faster recovery. For instance, at the most downstream coordinates in Fig. 28(a), the values of $\Sigma_1$ for $\lambda = 10$ become lower than those for $\lambda = 8$ and $\lambda = 6.45$, for which the process of recovery is still at an earlier stage. The turbulent transport terms in Figs. 28(b) and 28(c) were found less significant in comparison with radial advection. In contrast, the pressure gradient term is important across the near wake, giving a negative contribution to wake recovery, but declining within a short distance downstream, as shown in Fig. 28(d). Interestingly, this term was weakly affected by the value of $\lambda$, in comparison with the term of radial advection. As expected, viscous diffusion in Fig. 28(e) is practically negligible. Meanwhile, the modeled turbulent transport in Fig. 28(f) grows at downstream coordinates, due to grid coarsening away from the rotor. It shows a dependence on $\lambda$ which is similar to that observed for $\Sigma_1$, achieving higher values at more upstream coordinates for increasing tip speed ratios. Overall, the results in Fig. 28 point out that most

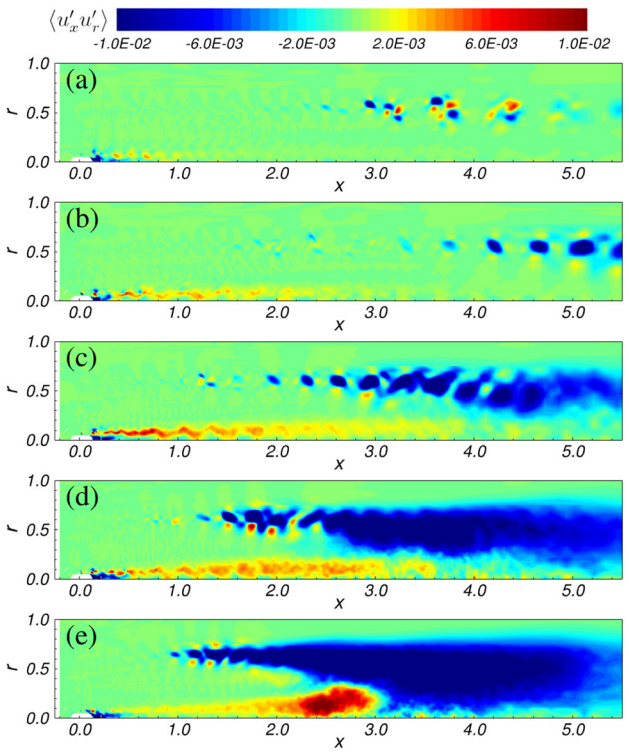


FIG. 22. Contours of the phase-averaged turbulent shear stress $\langle u'_x u'_r \rangle$ on a meridian plane through the axis of the turbine: (a) $\lambda = 4.00$, (b) $\lambda = 5.00$, (c) $\lambda = 6.45$, (d) $\lambda = 8.00$, and (e) $\lambda = 10.0$.

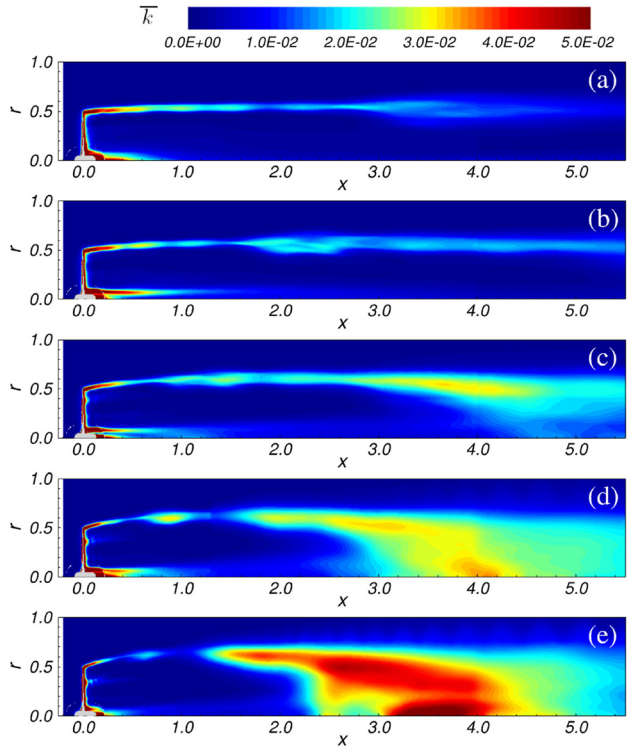


FIG. 24. Contours of turbulent kinetic energy on a meridian plane through the axis of the turbine: (a) $\lambda = 4.00$, (b) $\lambda = 5.00$, (c) $\lambda = 6.45$, (d) $\lambda = 8.00$, and (e) $\lambda = 10.0$.

recovery, as well as its strong dependence on $\lambda$, comes from radial advection of streamwise momentum: the breakup of the tip vortices allows the development of inward radial flows transporting momentum from the free stream into the wake core. These phenomena are accelerated by higher values of $\lambda$.

## V. CONCLUSIONS

The wake shed by the rotor of an axial-flow, hydrokinetic turbine was reproduced by detached eddy simulation, using an overlapping-grids technique. This strategy gave us flexibility in clustering grid points in the areas of large gradients only, allowing us to accurately resolve the dynamics of the tip vortices and their breakdown. The dependence of the wake recovery process on the tip speed ratio was analyzed, through its correlation with the phenomena of mutual inductance, coupling and eventual instability of the tip vortices shed by the rotor. Although earlier studies are available in the literature on eddy-resolving computations of axial-flow rotors, their analysis of the influence of the tip speed ratio is usually limited to the global parameters of performance or a narrow range of values of the rotational speed, without focusing on the process of wake recovery. In contrast, in this work, detached eddy simulation is exploited to gain insight on the wake features, the individual phenomena of pairing between the tip

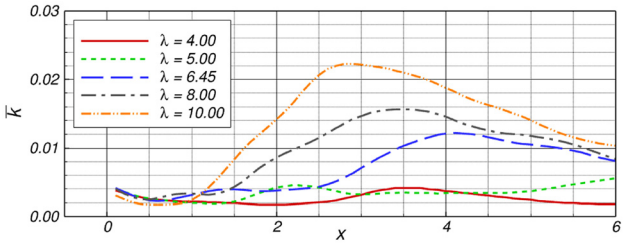


FIG. 23. Streamwise evolution of the turbulent kinetic energy. At each streamwise coordinate, average over cross sections ranging from the wake axis up to the radial location where $\overline{u}_x = 0.95U_\infty$.

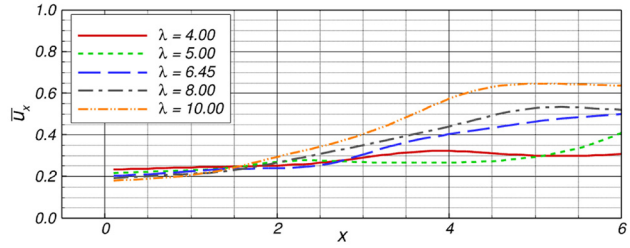


FIG. 25. Streamwise evolution of the time-averaged streamwise velocity. At each streamwise coordinate, average over cross sections ranging from the wake axis up to the radial location where $\overline{u}_x = 0.95U_\infty$.

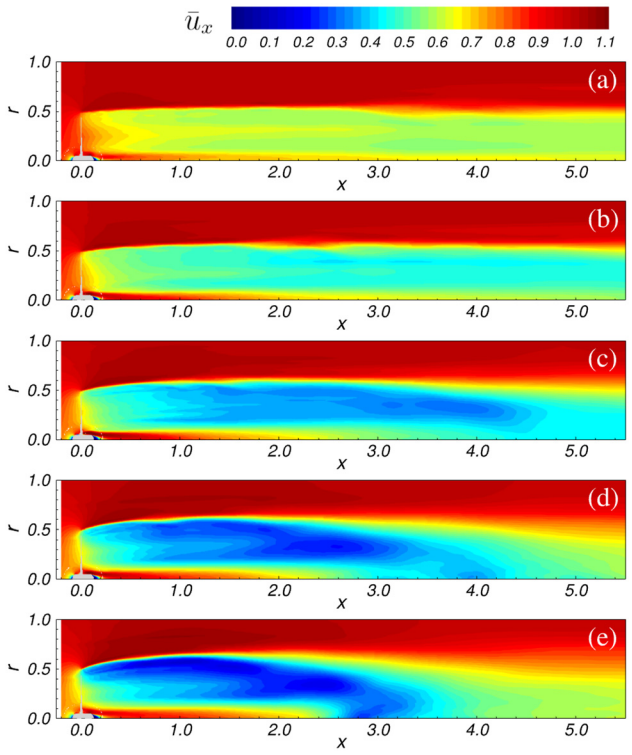


**FIG. 26.** Contours of time-averaged streamwise velocity on a meridian plane through the axis of the turbine: (a) $\lambda = 4.00$, (b) $\lambda = 5.00$, (c) $\lambda = 6.45$, (d) $\lambda = 8.00$, and (e) $\lambda = 10.0$.

vortices shed by the rotor and the mechanism of wake recovery downstream of their instability, across a wide range of values of tip speed ratio.

We found that, although higher values of tip speed ratio produced higher levels of momentum deficit just downstream of the rotor, its process of wake recovery was also faster. At higher rotational speeds the pitch of the tip vortices is smaller, resulting in a shorter distance between them, promoting mutual inductance phenomena. The present high-fidelity computations allowed us to isolate carefully each of these phenomena of mutual inductance, leading to paring events between tip vortices and their eventual instability and breakdown into turbulence.

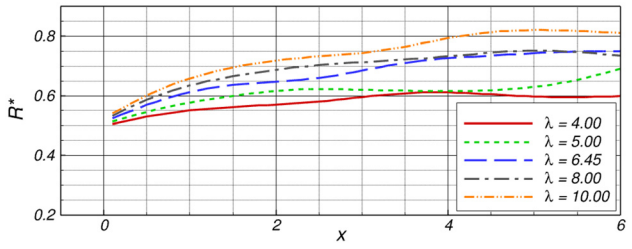


**FIG. 27.** Streamwise evolution of the radial coordinate, $R^*$, where $\bar{u}_x = 0.95U_\infty$, assumed as the wake boundary.

In their studies, Lignarolo *et al.*[16,17] pointed out that the tip vortices were incorrectly considered by the past literature as a source of turbulent mixing and resulting wake recovery. They found instead a strong correlation between wake recovery and the instability process of the tip vortices populating the outer boundary of the wake, since the latter triggers the penetration of higher-momentum fluid into the wake core from the free stream. Our results, spanning a number of values of tip speed ratio, are helpful to explain the source of the past, incorrect interpretation of the role of the tip vortices in the process of wake recovery, brought into question in the works by Lignarolo *et al.*[16,17] Stronger tip vortices at higher loads do not result *per se* in a more intense turbulent mixing, but they experience a faster instability, accelerating the process of wake recovery. The analysis we reported on the momentum balance equation showed that this process is mainly driven by radial advection, associated with the radial flows produced downstream of the breakup of the tip vortices from the gradient of streamwise velocity between the wake flow and the free stream. Therefore, the onset of intense radial advection phenomena occurs at more upstream coordinates for increasing values of $\lambda$, due to the faster instability of the helical tip vortices.

The implications of these results are important and not obvious: higher rotational speeds promote a faster wake recovery. Wind and hydrokinetic turbines are usually required to work in the wake of upstream turbines in configurations of multiple devices. Therefore, mutual interaction between them is an important limitation to their performance, since downstream turbines ingest the decelerated flow coming from the upstream ones. In addition, large flow structures, as the tip vortices, as long as they keep coherent, are detrimental to the structural stresses and fatigue experienced by downstream devices. Therefore, the relative distance between rows in a farm should be tuned to the expected, design tip speed ratio of operation of the turbines: higher rotational speeds allow for shorter distances between turbines, despite the larger levels of momentum deficit just downstream of them, thanks to their faster wake instability and recovery. These results are also in line with the outcomes of earlier studies, which demonstrate that the wake development of turbines in conditions of higher free-stream turbulence is faster.[8,88–90] This is explained by the faster instability of the tip vortices, accelerated by the free-stream turbulence.

The present study also pointed out that the process of instability of the tip vortices is characterized first by mutual inductance between them, leading to their pairing and the generation of a single helical vortex. Then, phenomena of auto-inductance between the spirals of this single vortex trigger instability and eventual breakup into smaller scales, promoting turbulent mixing and wake recovery. These findings indicate that also theoretical analyses focusing on the process of instability of isolated helical vortices[72,78–80] are relevant to the dynamics of the wake of actual axial-flow turbines. Although they shed multiple tip vortices (typically three, as in the present case), the later stage of the instability process involves also phenomena of auto-inductance of a single, larger helical vortex.

We should acknowledge that in the present work, a simplified geometry was considered, which is the rotor only of an axial-flow hydrokinetic turbine. In our future studies, we plan to include the effect of the supporting tower of the turbine as well as that of the free-surface. The comparison with the results of this study will help us in isolating those effects on the phenomena of instability of the tip vortices and the resulting process of wake recovery.

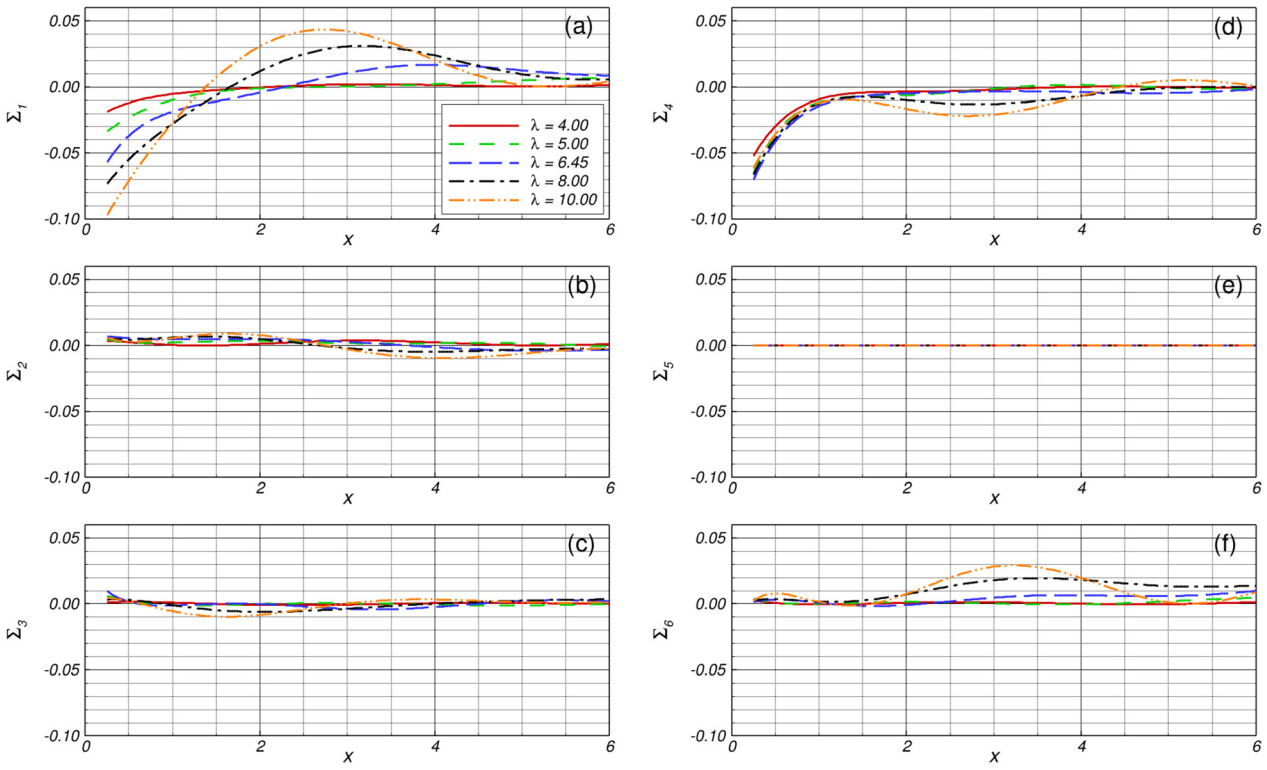


**FIG. 28.** Streamwise evolution of the six terms at the right hand side of Eq. (8): (a) radial advection, (b) radial turbulent transport, (c) streamwise turbulent transport, (d) pressure gradient, (e) viscous diffusion, and (f) modeled turbulent transport. At each streamwise coordinate, average over cross sections ranging from the wake axis up to the radial location where $\overline{u}_x = 0.95U_\infty$.



## ACKNOWLEDGMENTS

This work received funds from the UK Engineering and Physical Sciences Research Council (EPSRC) (Grant No. EP/V009443/1).

## AUTHOR DECLARATIONS

### Conflict of Interest

The authors have no conflicts to disclose.

### Author Contributions

**Antonio Posa:** Conceptualization (equal); Data curation (supporting); Formal analysis (equal); Investigation (equal); Methodology (supporting); Software (supporting); Supervision (equal); Validation (equal); Visualization (supporting); Writing – original draft (lead); Writing – review & editing (lead). **Ignazio Maria Viola:** Conceptualization (equal); Formal analysis (equal); Funding acquisition (lead); Investigation (equal); Methodology (supporting); Project administration (lead); Resources (lead); Supervision (equal); Validation (equal); Visualization (supporting); Writing – original draft (supporting); Writing – review & editing (supporting). **Riccardo Broglia:** Conceptualization (equal); Data curation (lead); Formal analysis (equal); Investigation (equal); Methodology (lead); Software (lead); Supervision (equal); Validation (equal); Visualization (lead); Writing – original draft (supporting); Writing – review & editing (supporting).

## DATA AVAILABILITY

The data that support the findings of this study are available from the corresponding author upon reasonable request.

## REFERENCES

[1]P. Ouro, L. Ramírez, and M. Harrold, "Analysis of array spacing on tidal stream turbine farm performance using large-eddy simulation," J. Fluids Struct. **91**, 102732 (2019).
[2]P. Ouro and T. Nishino, "Performance and wake characteristics of tidal turbines in an infinitely large array," J. Fluid Mech. **925**, A30 (2021).
[3]J. Han, J. Jung, and J. Hwang, "Optimal configuration of a tidal current turbine farm in a shallow channel," Ocean Eng. **220**, 108395 (2021).
[4]P. Modali, A. Vinod, and A. Banerjee, "Towards a better understanding of yawed turbine wake for efficient wake steering in tidal arrays," Renewable Energy **177**, 482–494 (2021).
[5]V. Nago, I. Santos, M. Gbedjinou, J. Mensah, G. Tiago Filho, R. Camacho, and R. Barros, "A literature review on wake dissipation length of hydrokinetic turbines as a guide for turbine array configuration," Ocean Eng. **259**, 111863 (2022).
[6]A. Posa, R. Broglia, and E. Balaras, "Recovery in the wake of in-line axial-flow rotors," Phys. Fluids **34**, 045104 (2022).

[7]A. Posa and R. Broglia, "Analysis of the momentum recovery in the wake of aligned axial-flow hydrokinetic turbines," Phys. Fluids **34**, 105130 (2022).
[8]P. Mycek, B. Gaurier, G. Germain, G. Pinon, and E. Rivoalen, "Experimental study of the turbulence intensity effects on marine current turbines behaviour. Part II: Two interacting turbines," Renewable Energy **68**, 876–892 (2014).
[9]M. Nuernberg and L. Tao, "Experimental study of wake characteristics in tidal turbine arrays," Renewable Energy **127**, 168–181 (2018).
[10]M. Nuernberg and L. Tao, "Three dimensional tidal turbine array simulations using OpenFOAM with dynamic mesh," Ocean Eng. **147**, 629–646 (2018).
[11]C. Gotelli, M. Musa, M. Guala, and C. Escauriaza, "Experimental and numerical investigation of wake interactions of marine hydrokinetic turbines," Energies **12**, 3188 (2019).
[12]V. Okulov, I. Naumov, I. Kabardin, I. Litvinov, D. Markovich, R. Mikkelsen, J. Sørensen, S. Alekseenko, and D. Wood, "Experiments on line arrays of horizontal-axis hydroturbines," Renewable Energy **163**, 15–21 (2021).
[13]A. Posa and R. Broglia, "Momentum recovery downstream of an axial-flow hydrokinetic turbine," Renewable Energy **170**, 1275–1291 (2021).
[14]A. Posa and R. Broglia, "Characterization of the turbulent wake of an axial-flow hydrokinetic turbine via large-eddy simulation," Comput. Fluids **216**, 104815 (2021).
[15]A. Posa, R. Broglia, and E. Balaras, "Instability of the tip vortices shed by an axial-flow turbine in uniform flow," J. Fluid Mech. **920**, A19 (2021).
[16]L. Lignarolo, D. Ragni, C. Krishnaswami, Q. Chen, C. Simão Ferreira, and G. van Bussel, "Experimental analysis of the wake of a horizontal-axis wind-turbine model," Renewable Energy **70**, 31–46 (2014).
[17]L. Lignarolo, D. Ragni, F. Scarano, C. Simão Ferreira, and G. Van Bussel, "Tip-vortex instability and turbulent mixing in wind-turbine wakes," J. Fluid Mech. **781**, 467–493 (2015).
[18]K. Brown, D. Houck, D. Maniaci, C. Westergaard, and C. Kelley, "Accelerated wind-turbine wake recovery through actuation of the tip-vortex instability," AIAA J. **60**, 3298–3310 (2022).
[19]X. Zhu, C. Sun, H. Ouyang, and Z. Du, "Numerical investigation of the effect of towers and nacelles on the near wake of a horizontal-axis wind turbine model," Energy **238**, 121782 (2022).
[20]Q. Guo, L. Zhou, and Z. Wang, "Comparison of BEM-CFD and full rotor geometry simulations for the performance and flow field of a marine current turbine," Renewable Energy **75**, 640–648 (2015).
[21]P. A. S. F. Silva, T. F. De Oliveira, A. C. P. Brasil Junior, and J. R. P. Vaz, "Numerical study of wake characteristics in a horizontal-axis hydrokinetic turbine," An. Acad. Bras. Ciênc. **88**, 2441–2456 (2016).
[22]S. A. Abdulqadir, H. Iacovides, and A. Nasser, "The physical modelling and aerodynamics of turbulent flows around horizontal axis wind turbines," Energy **119**, 767–799 (2017).
[23]T. Javaherchi, N. Stelzenmuller, and A. Aliseda, "Experimental and numerical analysis of the performance and wake of a scale-model horizontal axis marine hydrokinetic turbine," J. Renewable Sustainable Energy **9**, 044504 (2017).
[24]P. Pyakurel, W. Tian, J. H. VanZwieten, and M. Dhanak, "Characterization of the mean flow field in the far wake region behind ocean current turbines," J. Ocean Eng. Mar. Energy **3**, 113–123 (2017).
[25]S. Salunkhe, O. E. Fajri, S. Bhushan, D. Thompson, D. O'Doherty, T. O'Doherty, and A. Mason-Jones, "Validation of tidal stream turbinewake predictions and analysis of wake recovery mechanism," J. Mar. Sci. Eng. **7**, 362 (2019).
[26]M. M. Amiri, M. Shadman, and S. F. Estefen, "URANS simulations of a horizontal axis wind turbine under stall condition using Reynolds stress turbulence models," Energy **213**, 118766 (2020).
[27]O. El Fajri, S. Bhushan, D. Thompson, and T. O'Doherty, "Numerical investigation of shallow-water effects on hydrokinetic turbine wake recovery," Int. J. Mar. Energy J. **3**, 25–35 (2020).
[28]A. Abutunis, M. Fal, O. Fashanu, K. Chandrashekhara, and L. Duan, "Coaxial horizontal axis hydrokinetic turbine system: Numerical modeling and performance optimization," J. Renewable Sustainable Energy **13**, 024502 (2021).
[29]M. Faizan, S. Badshah, M. Badshah, and B. Haider, "Performance and wake analysis of horizontal axis tidal current turbine using improved delayed detached eddy simulation," Renewable Energy **184**, 740–752 (2022).
[30]Y. Cai, H. Zhao, X. Li, and Y. Liu, "Effects of yawed inflow and blade-tower interaction on the aerodynamic and wake characteristics of a horizontal-axis wind turbine," Energy **264**, 126246 (2023).
[31]M. Macías, R. C. F. Mendes, M. Pereira, I. Dobrev, T. F. Oliveira, and A. C. P. Brasil Junior, "Wake characteristics in high solidity horizontal axis hydrokinetic turbines: A comparative study between experimental techniques and numerical simulations," J. Braz. Soc. Mech. Sci. Eng. **46**, 24 (2024).
[32]M. Ye, H.-C. Chen, and A. Koop, "High-fidelity CFD simulations for the wake characteristics of the NTNU BT1 wind turbine," Energy **265**, 126285 (2023).
[33]P. Romero-Gomez and M. Richmond, "Simulating blade-strike on fish passing through marine hydrokinetic turbines," Renewable Energy **71**, 401–413 (2014).
[34]M. Richmond, S. Harding, and P. Romero-Gomez, "Numerical performance analysis of acoustic doppler velocity profilers in the wake of an axial-flow marine hydrokinetic turbine," Int. J. Mar. Energy **11**, 50–70 (2015).
[35]M. Boudreau and G. Dumas, "Comparison of the wake recovery of the axial-flow and cross-flow turbine concepts," J. Wind Eng. Ind. Aerodyn. **165**, 137–152 (2017).
[36]G. Chen, X.-B. Li, and X.-F. Liang, "IDDES simulation of the performance and wake dynamics of the wind turbines under different turbulent inflow conditions," Energy **238**, 121772 (2022).
[37]S. Kang, I. Borazjani, J. Colby, and F. Sotiropoulos, "Numerical simulation of 3D flow past a real-life marine hydrokinetic turbine," Adv. Water Resour. **39**, 33–43 (2012).
[38]S. Kang, X. Yang, and F. Sotiropoulos, "On the onset of wake meandering for an axial flow turbine in a turbulent open channel flow," J. Fluid Mech. **744**, 376–403 (2014).
[39]S. Chawdhary, C. Hill, X. Yang, M. Guala, D. Corren, J. Colby, and F. Sotiropoulos, "Wake characteristics of a TriFrame of axial-flow hydrokinetic turbines," Renewable Energy **109**, 332–345 (2017).
[40]P. Ouro, M. Harrold, T. Stoesser, and P. Bromley, "Hydrodynamic loadings on a horizontal axis tidal turbine prototype," J. Fluids Struct. **71**, 78–95 (2017).
[41]P. Ouro and T. Stoesser, "Impact of environmental turbulence on the performance and loadings of a tidal stream turbine," Flow. Turbul. Combust. **102**, 613–639 (2019).
[42]G. Dong, J. Qin, Z. Li, and X. Yang, "Characteristics of wind turbine wakes for different blade designs," J. Fluid Mech. **965**, A15 (2023).
[43]S. Hurubi, T. Stallard, P. Stansby, H. Mullings, and P. Ouro, "Characterisation of turbulent flow and the wake of a tidal stream turbine in proximity to a ridge," in *Proceedings of the 15th European Wave and Tidal Energy Conference, 3–7 September 2023* (University of the Basque Country, Bilbao, 2023), Vol. 15.
[44]Y. Qian, Y. Zhang, Y. Sun, H. Zhang, Z. Zhang, and C. Li, "Experimental and numerical investigations on the performance and wake characteristics of a tidal turbine under yaw," Ocean Eng. **289**, 116276 (2023).
[45]C. Santoni, A. Khosronejad, X. Yang, P. Seiler, and F. Sotiropoulos, "Coupling turbulent flow with blade aeroelastics and control modules in large-eddy simulation of utility-scale wind turbines," Phys. Fluids **35**, 015140 (2023).
[46]T. Stallard, H. Mullings, S. Draycott, and P. Ouro, "Large-eddy simulations of interaction between surface waves and a tidal turbine wake in a turbulent channel," in *Proceedings of the 15th European Wave and Tidal Energy Conference, 3–7 September 2023* (University of the Basque Country, Bilbao, 2023), Vol. 15.
[47]S. Xu, T. Zhuang, W. Zhao, and D. Wan, "Numerical investigation of aerodynamic responses and wake characteristics of a floating offshore wind turbine under atmospheric boundary layer inflows," Ocean Eng. **279**, 114527 (2023).
[48]C. Niebuhr, S. Schmidt, M. van Dijk, L. Smith, and V. Neary, "A review of commercial numerical modelling approaches for axial hydrokinetic turbine wake analysis in channel flow," Renewable Sustainable Energy Rev. **158**, 112151 (2022).
[49]O. El Fajri, J. Bowman, S. Bhushan, D. Thompson, and T. O'Doherty, "Numerical study of the effect of tip-speed ratio on hydrokinetic turbine wake recovery," Renewable Energy **182**, 725–750 (2022).
[50]W. Tian, J. H. VanZwieten, P. Pyakurel, and Y. Li, "Influences of yaw angle and turbulence intensity on the performance of a 20 kW in-stream hydrokinetic turbine," Energy **111**, 104–116 (2016).
[51]P. García Regodeseves and C. Santolaria Morros, "Unsteady numerical investigation of the full geometry of a horizontal axis wind turbine: Flow through the rotor and wake," Energy **202**, 117674 (2020).
[52]M. S. Siddiqui, M. H. Khalid, A. W. Badar, M. Saeed, and T. Asim, "Parametric analysis using CFD to study the impact of geometric and numerical modeling on the performance of a small scale horizontal axis wind turbine," Energies **15**, 505 (2022).

[53]F. Di Felice, A. Capone, G. P. Romano, and F. Alves Pereira, "Experimental study of the turbulent flow in the wake of a horizontal axis tidal current turbine," Renewable Energy **212**, 17–34 (2023).
[54]M. Bourhis, M. Pereira, and F. Ravelet, "Experimental investigation of the effects of the Reynolds number on the performance and near wake of a wind turbine," Renewable Energy **209**, 63–70 (2023).
[55]N. Biswas and O. R. Buxton, "Effect of tip speed ratio on coherent dynamics in the near wake of a model wind turbine," J. Fluid Mech. **979**, A34 (2024).
[56]M. Felli, R. Camussi, and F. Di Felice, "Mechanisms of evolution of the propeller wake in the transition and far fields," J. Fluid Mech. **682**, 5–53 (2011).
[57]A. Di Mascio, R. Broglia, and B. Favini, "A second order Godunov–type scheme for naval hydrodynamics," in *Godunov Methods: Theory and Applications* (Kluwer Academic/Plenum Publishers, Boston, MA, 2001), pp. 253–261.
[58]A. Di Mascio, R. Broglia, and R. Muscari, "Prediction of hydrodynamic coefficients of ship hulls by high-order Godunov-type methods," J. Mar. Sci. Technol. **14**, 19–29 (2009).
[59]R. Broglia, S. Zaghi, R. Muscari, and F. Salvadore, "Enabling hydrodynamics solver for efficient parallel simulations," in *Proceedings of the 2014 International Conference on High Performance Computing and Simulation, HPCS 2014* (IEEE, 2014), pp. 803–810.
[60]P. R. Spalart and S. R. Allmaras, "A one–equation turbulence model for aerodynamic flows," Rech. Aerosp. **1**, 5–21 (1994).
[61]P. Spalart, W.-H. Jou, M. Strelets, and S. Allmaras, "Comments on the feasibility of les for wings, and on a hybrid rans/les approach," in *Advances in DNS/LES: Proceedings of the First AFOSR International Conference on DNS/LES* (Greyden Press, 1997), pp. 137–147.
[62]J. Smagorinsky, "General circulation experiments with the primitive equations: I. The basic experiment," Mon. Weather Rev. **91**, 99–164 (1963).
[63]A. Posa and R. Broglia, "An immersed boundary method coupled with a dynamic overlapping-grids strategy," Comput. Fluids **191**, 104250 (2019).
[64]A. Di Mascio, R. Muscari, and R. Broglia, "An overlapping grids approach for moving bodies problems," in *Proceedings of 16th International Offshore and Polar Engineering Conference* (the International Society of Offshore and Polar Engineers, San Francisco, CA, 2006).
[65]S. Zaghi, A. Di Mascio, R. Broglia, and R. Muscari, "Application of dynamic overlapping grids to the simulation of the flow around a fully-appended submarine," Math. Comput. Simul. **116**, 75–88 (2015).
[66]A. Chorin, "A numerical method for solving incompressible viscous flow problems," J. Comput. Phys. **2**, 12–26 (1967).
[67]B. Favini, R. Broglia, and A. Di Mascio, "Multi–grid acceleration of second order ENO schemes from low subsonic to high supersonic flows," Numer. Methods Fluids **23**, 589–606 (1996).
[68]S. Draycott, G. Payne, J. Steynor, A. Nambiar, B. Sellar, and V. Venugopal, "An experimental investigation into non-linear wave loading on horizontal axis tidal turbines," J. Fluids Struct. **84**, 199–217 (2019).
[69]T. Xing and F. Stern, "Factors of safety for Richardson extrapolation," J. Fluids Eng., Trans. ASME **132**, 061403 (2010).
[70]J. Hunt, A. Wray, and P. Moin, "Eddies, streams, and convergence zones in turbulent flows," in *Center for Turbulence Research, Proceedings of the Summer Program 1988* (Stanford University, 1988), pp. 193–208.
[71]J. Jeong and F. Hussain, "On the identification of a vortex," J. Fluid Mech. **285**, 69–94 (1995).
[72]S. Widnall, "The stability of a helical vortex filament," J. Fluid Mech. **54**, 641–663 (1972).
[73]A. Posa, R. Broglia, and E. Balaras, "The dynamics of the tip and hub vortices shed by a propeller: Eulerian and Lagrangian approaches," Comput. Fluids **236**, 105313 (2022).
[74]A. Posa, "Dependence of tip and hub vortices shed by a propeller with winglets on its load conditions," Phys. Fluids **34**, 105107 (2022).
[75]A. Posa and R. Broglia, "Influence by the hub vortex on the instability of the tip vortices shed by propellers with and without winglets," Phys. Fluids **34**, 115115 (2022).
[76]A. Posa, "The dynamics of the tip vortices shed by a tip-loaded propeller with winglets," J. Fluid Mech. **951**, A25 (2022).
[77]A. Posa, "Anisotropy of turbulence at the core of the tip and hub vortices shed by a marine propeller," J. Fluid Mech. **969**, A23 (2023).
[78]H. Quaranta, H. Bolnot, and T. Leweke, "Long-wave instability of a helical vortex," J. Fluid Mech. **780**, 687–716 (2015).
[79]V. Okulov and J. Sørensen, "The self-induced motion of a helical vortex," J. Fluid Mech. **883**, A5 (2020).
[80]C. Li, Y. Liu, M. Wan, S. Chen, and D. Yue, "The instability of a helical vortex filament under a free surface," J. Fluid Mech. **937**, A21 (2022).
[81]P. Bachant and M. Wosnik, "Characterising the near-wake of a cross-flow turbine," J. Turbul. **16**, 392–410 (2015).
[82]P. Bachant and M. Wosnik, "Effects of Reynolds number on the energy conversion and near-wake dynamics of a high solidity vertical-axis cross-flow turbine," Energies **9**, 73 (2016).
[83]P. Bachant and M. Wosnik, "Modeling the near-wake of a vertical-axis cross-flow turbine with 2-D and 3-D RANS," J. Renewable Sustainable Energy **8**, 053311 (2016).
[84]P. Ouro, S. Runge, Q. Luo, and T. Stoesser, "Three-dimensionality of the wake recovery behind a vertical axis turbine," Renewable Energy **133**, 1066–1077 (2019).
[85]A. Posa, "Dependence of the wake recovery downstream of a vertical axis wind turbine on its dynamic solidity," J. Wind Eng. Ind. Aerodyn. **202**, 104212 (2020).
[86]A. Posa, "Analysis of momentum recovery within the near wake of a cross-flow turbine using large eddy simulation," Comput. Fluids **231**, 105178 (2021).
[87]A. Posa, "Wake characterization of paired cross-flow turbines," Renewable Energy **196**, 1064–1094 (2022).
[88]P. Mycek, B. Gaurier, G. Germain, G. Pinon, and E. Rivoalen, "Experimental study of the turbulence intensity effects on marine current turbines behaviour. Part I: One single turbine," Renewable Energy **66**, 729–746 (2014).
[89]A. Vinod and A. Banerjee, "Performance and near-wake characterization of a tidal current turbine in elevated levels of free stream turbulence," Appl. Energy **254**, 113639 (2019).
[90]B. Gaurier, C. Carlier, G. Germain, G. Pinon, and E. Rivoalen, "Three tidal turbines in interaction: An experimental study of turbulence intensity effects on wakes and turbine performance," Renewable Energy **148**, 1150–1164 (2020).